Gold, Silver, and Electrum Electroless Plating on Additively Manufactured Laser Powder-Bed Fusion AlSi10Mg Parts: A Review

Dana Ashkenazi [1],*[ID]**, Alexandra Inberg** [2]**, Yosi Shacham-Diamand** [2,3][ID] **and Adin Stern** [4,5]

[1] School of Mechanical Engineering, Tel Aviv University, Ramat Aviv 6997801, Israel
[2] School of Electrical Engineering, Tel Aviv University, Ramat Aviv 6997801, Israel; inberg@tauex.tau.ac.il (A.I.); yosish@tauex.tau.ac.il (Y.S.-D.)
[3] Department of Materials Science and Engineering, Tel Aviv University, Ramat Aviv 6997801, Israel
[4] Department of Mechanical Engineering, Afeka Academic College of Engineering, Tel Aviv 6910717, Israel; aandls@gmail.com
[5] Department of Materials Engineering, Ben-Gurion University of the Negev, Beer Sheva 8410501, Israel
*   Correspondence: danaa@tauex.tau.ac.il; Tel.: +972-3-6405579

Abstract: Additive manufacturing (AM) revolutionary technologies open new opportunities and challenges. They allow low-cost manufacturing of parts with complex geometries and short time-to-market of products that can be exclusively customized. Additive manufactured parts often need post-printing surface modification. This study aims to review novel environmental-friendly surface finishing process of 3D-printed AlSi10Mg parts by electroless deposition of gold, silver, and gold–silver alloy (e.g., electrum) and to propose a full process methodology suitable for effective metallization. This deposition technique is simple and low cost method, allowing the metallization of both conductive and insulating materials. The AlSi10Mg parts were produced by the additive manufacturing laser powder bed fusion (AM-LPBF) process. Gold, silver, and their alloys were chosen as coatings due to their esthetic appearance, good corrosion resistance, and excellent electrical and thermal conductivity. The metals were deposited on 3D-printed disk-shaped specimens at 80 and 90 °C using a dedicated surface activation method where special functionalization of the printed AlSi10Mg was performed to assure a uniform catalytic surface yielding a good adhesion of the deposited metal to the substrate. Various methods were used to examine the coating quality, including light microscopy, optical profilometry, XRD, X-ray fluorescence, SEM–energy-dispersive spectroscopy (EDS), focused ion beam (FIB)-SEM, and XPS analyses. The results indicate that the developed coatings yield satisfactory quality, and the suggested surface finishing process can be used for many AM products and applications.

Keywords: additive manufacturing; AlSi10Mg; electroless deposition; gold–silver coatings; laser powder bed fusion; surface modification

1. Introduction

1.1. Additive Manufacturing

The AlSi10Mg alloy belongs to the hypoeutectic aluminum–silicon group [1]. This alloy has good fluidity accompanied by low shrinkage, making it an important cast alloy with excellent weldability. AlSi10Mg contains about 0.4 wt.% Mg, making the alloy a heat treatable material that responds to the precipitation hardening processes [2]. Adding Mg to the Al-Si alloy allows the formation of Mg_2Si precipitations, which considerably strengthens the matrix without reducing other mechanical properties [1]. The alloy is also hardened by rapid solidification, where high cooling rates are imposed, refining the microstructure [3].

A high strength/weight ratio, lighter weights, and higher corrosion resistance of aluminum alloys enable their easy replacement for other materials in different engineering applications [4]. Recently, additive manufacturing (AM) technologies have been applied for

fabricating lightweight parts of simple and complex shapes to be used by different engineering sectors. Additive manufacturing has been used for various materials, including metals and their alloys. The overall AlSi10Mg alloy properties make the material ideally suitable for processing using the laser powder bed fusion (LPBF) AM technology and adoption of the alloy by many industries, including the aerospace and automotive sectors [4–6]. To ensure the high quality of printed specimens, it is essential to understand the impact of both the LPBF process parameters and the material feedstock properties on the quality of the parts [7], including the plastic anisotropic behavior; a notable lower ductility is typically observed for the vertical printed tensile samples when compared to their respective horizontal samples [4–8]. Namely, the study of the unique LPBF solidification conditions and the material's thermal history may lead to the understanding of the characteristic defects (porosity, hot cracking phenomena, and surface roughness), observed in AlSi10Mg alloy components produced by the LPBF technique [6,7]. The surface quality depends on the intrinsic material properties as well as on the scan strategies during printing, i.e., contour scans and skywriting scans. The roughness is typically caused by the parallel running welding beads and by stairs effect [9].

So far, many studies have investigated the influence of the LPBF process parameters (i.e., thickness of the printed layer, laser power, scanning speed, build-strategy, chamber atmosphere etc.) on the quality of the LPBF parts. For example, Yang studied the influence of process parameters, such as laser power and scanning speed, on the vertical surface roughness of the AlSi10Mg parts fabricated by LPBF process [9]. Steuben et al. 2019 discussed the use of a computational enriched analytical solution method (EASM) for AM modeling and simulation in order to predict the influence of process parameters on the properties and associated functional performance of the LPBF parts [10]. Understanding the influence of main LPBF processing parameters on the surface roughness of AM components can be used for additional process optimization [11]. Surface post-processing techniques, such as heat treatment, shot peening, polishing, sand blasting, and coatings [12], and the resulting part qualities for the AlSi10Mg alloy have been discussed before [13–15]. Yet, surface post-processing techniques increase the production time and cost [12].

In this paper, we add more information on post-AM surface modification, presenting a novel finishing process and suggesting a methodology for electroless plating of silver, gold, and their alloys as a method to improve surface quality, both physical and ornamental.

1.2. Electroless Plating of Gold, Silver and Au–Ag Alloys

The quality of the surface finish of 3D-printed parts produced by the AM-LPBF is occasionally unsuitable for applications demanding, for example, low roughness and uniformity. Therefore, additional post-AM surface modification processes, such as machine finishing techniques and coatings, are frequently applied [16]. Different metallic coatings are often used, improving electrical, thermal, optical, and mechanical properties, as well as erosion and corrosion resistance, and achieving a decorative appearance of the AM-printed parts. See, for example, the paper by Kuo et al. 2017, which specifically stated that improving the surface quality of additive manufactured parts by minimizing the roughness of the surface is a promising engineering topic, which can be achieved by coating the printed surface [17]. The quality of the coating depends on various factors, including the parameters of the AM process, e.g., the position and orientation, and the presence of external defects, the part's surface roughness, and the cleaning process of the surface before coating [18].

Metal deposition of thin films is accomplished by either physical, chemical, or electrochemical methods, such as physical vapor deposition (PVD), chemical vapor deposition (CVD), and electrochemical deposition (ECD). Electroless deposition (ELD), which is an electrochemical method, is promising for printed metal surface finishing, since it is rather simple, relatively (to other methods) inexpensive and, most importantly, it yields good results [19]. For instant, ELD may be used for the production of 3D-printed micro circuitries for structural electronic devices [16].

The electroless plating process is based on the simultaneous metal reduction and reducing-agent oxidation on an activated surface, where the heterogeneous reactions continue in an autocatalytic form until the depletion of one of the components (or both), assuming the bath conditions, such as pH and temperature, are kept unchanged [19]. The electrons for the chemical reduction are provided by the oxidation of a reducing agent [20]. Hence, the electroless plating occurs without the use of an external current source, and therefore, it requires a relatively simple bath and control and support units. The electroless process occurs in an aqueous bath, which is relatively simpler than that of other metal and alloy deposition such as vacuum-based PVD and CVD equipment [21–25]. In this self-initiating auto-catalytic process, a catalytic substrate is dipped into an aqueous solution containing metal ions (typically in a complex form), reducing agents, and pH adjustment components [19,23]. In a few cases, the bath may include also special additives in a minute amount for special functions such as brightening or leveling [19]. ELD is a controlled method, which has been used industrially for many years, it operates at a moderately low temperature (<100 °C), and allows high selectivity depositions on both conductive and non-conductive surfaces [20–23]. The ELD technique provides relatively uniform thickness of metal and alloy deposits. For example, according to Shacham-Diamand et al. 2000 [26] and Shukla et al. 2014 [27], electroless silver deposition produces high-quality coating with a thickness of up to about 1 μm [26–28]. This technique is particularly effective in the case of deep pores and rough surfaces [28].

ELD manufacturing of nickel–phosphorus (Ni–P) was developed by Brenner and Riddell [29] in the mid-1940s, and since then, it has been frequently used in numerous industries as a protective layer [30]. For example, Ni–P film is commonly applied atop porous surfaces [31]. Crystallization and phase transformation processes of ELD Ni–P film during thermal processing have roles in determining the material properties [32]. By applying an ELD Ni–P layer on top of an aluminum alloy substrate, the material properties, such as corrosion resistance, wear resistance, and hardness may be significantly improved [33,34]. In addition, according to Asher et al. 2009, self-assembled monolayers (SAMs), such as functional silanes SAMs, may also be applied in order to improve the metal adhesion to oxidized surfaces [21].

Gold and silver were among the first metals used by ancient societies; both are transition metals with shiny appearances [35]. Gold and silver have excellent corrosion resistance, they are soft, ductile, and malleable metals with superb reflectivity and high electrical and thermal conductivity [36,37]. Electrum, a gold–silver alloy that usually contains 60 wt.%–80 wt.% Au and 20 wt.%–40 wt.% Ag [38], was initially used during the first millennium BCE. The first known metal coins used in antiquity, which were dated to 630–620 BCE, were made of electrum [35]. Some ancient electrum items contain more than 20 wt.%–40 wt.% silver [39,40]. For instance, according to Ashkenazi et al. 2017, the fourth century BCE electrum bar with granules from the Nablus Hoard was composed of 21.6 wt.%–64.5 wt.% Au and 35.5 wt.%–77.4 wt.% Ag [35].

Applying gold, silver, and electrum coatings over objects made of aluminum alloys can efficiently shield the parts against corrosion in many severe environments, for instance, protection against pitting corrosion of Al in a surrounding of NaCl solutions [36]. Silver deposition is often used to coat aluminum micro-mirrors when high reflectivity is needed in the visible light, near infrared light, and radio frequency wavelengths [41].

There are different industrial gold and silver ELD processes employing various formulations. However, the associated published technological information is limited as a result of commercial confidentiality. In addition, industrial processes commonly use environmentally hazardous materials such as cyanide compounds [42,43]. A few studies have been published on the electrochemical deposition of Au–Ag alloy films [44–47]. However, no formulations of ELD for Au–Ag alloy coatings have been published in the open literature before Inberg et al. 2020 [48].

Electroless gold, silver, and electrum coatings can be useful to improve the properties of AM-LPBF parts for many applications. For example, in some AM-LPBF AlSi10Mg

items, additional coatings may be needed to improve electrical and thermal conductivity or to achieve a certain aesthetic appearance. The shiny and luxurious appearance of gold [43], silver [42], and electrum [48] plating can be used in numerous applications, among them replicas of ancient objects, such as valuable coins for museum presentations [42,43]. ELD of gold [49] and silver [50] metals can also be applied over AM fused filament fabrication (AM-FFF) acrylonitrile butadiene styrene (ABS) polymer objects when an appropriate chemical pretreatment process of the surface is done [49,50].

The objective of this research is to study the use of a novel environmentally friendly ELD finishing process by gold, silver, and electrum, of AM-LPBF AlSi10Mg parts, as a part of their post-printing surface modification. In addition, based on previous work of Dresler et al. 2019 [42] and Inberg et al. 2020 [43,48], this review aims to propose a methodology for effective Au, Ag, and Au–Ag ELD coatings of AM-LPBF AlSi10Mg objects. We should point out that one of the highlights of the technologies described here is the surface activation method. Since electroless plating is an autocatalytic process, it requires a high-quality catalytic surface to initiate the deposition. Any defect in the pre-deposition process will show up in the final coating. Hence, the SAM surface modification, which was developed by Osaka and his research group [51], may contribute to the success of the proposed process. That method was developed originally for a silicon dioxide surface as a barrier layer. However, it can be applied for other oxidized materials, in our case to AlSi10Mg, allowing the formation of a stable bond between the SAM adhesion layer and the substrate.

2. Materials and Experimental Methods

2.1. AM-LPBF AlSi10Mg Disk-Shaped Specimens

The 26 mm diameter disk-shaped samples (Figure 1) and coin replica specimens were fabricated with an EOSINT M 280 instrument (EOS Company, Krailling, Germany), which uses the conventional AM-LPBF process. The samples were additively built directly from computer-aided design (CAD) data (Figure 1a–c). The disk-shaped samples, which were designed to simulate the look and geometry of ancient metal coins, consist of an obverse side with two steps (1 mm height each) and a reverse side with planar surface. The printing compartment was controlled under argon flow (up to maximal oxygen content of 0.12 %), which lowers the alloy oxidation during the process. The chemical composition of the as-received AlSi10Mg feedstock is shown in Table 1. The particle-size distribution showed particles ranging between 15 and 75 μm. Scanning electron micrographs reveal that the powders show an irregular particles shape with a low quantity of elongated particles and only a limited satellite attachment on the powder surface (Figure 2a). The powder's microstructure (Figure 2b) consists of a primary α-Al matrix with cellular-dendritic and eutectic microstructures with very fine fibrous Si; some scattered micron size porosity is also evident [42].
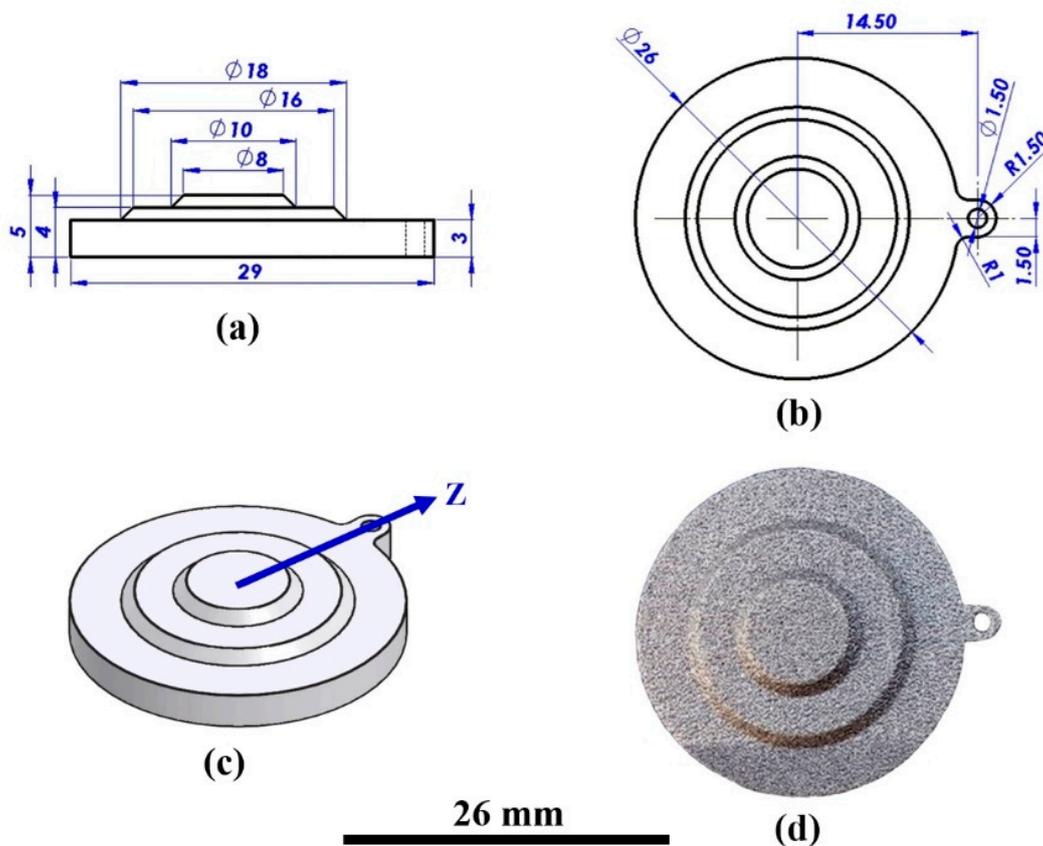
Figure 1. The disk-shaped configuration: (**a**) front view computer-aided design (CAD) model; (**b**) top view CAD model; (**c**) isometric view CAD model, showing the Z-direction (blue arrow); and (**d**) typical additive manufacturing laser powder-bed fusion (AM-LPBF) 3D-printed AlSi10Mg specimen.

Table 1. The chemical composition of the AlSi10Mg powder: Basic standard: BS EN 1706:2020.

Alloy	Composition (wt %)							
	Si	**Mg**	**Fe**	**Cu, Mn, Zn, Ni, Pn, Sn**	**Ti**	**Al**	**O**	**N**
1706	9.0–11.0	0.20–0.45	≤0.55	≤0.1	≤0.15	Bal.	N.A.	N.A.

The specimens (Figure 1d) were printed with a 400 W continuous Yb:YAG fiber laser beam (laser beam diameter ≈100 μm) along the vertical Z-axis (Figure 1c) with a scanning velocity of ≈1 m·s^{-1}. The temperature of the 250 mm × 250 mm × 300 mm build-platform was about 35 °C through the manufacturing process. An average layer thickness of ≈60 μm prior to melting led to a solid layer thickness of ≈30 μm after solidification. A post T5 heat treatment was performed on the as-built specimens, i.e., holding the disk-shape specimens for 2 h at 300 °C in an air-furnace followed by furnace cooling [42].
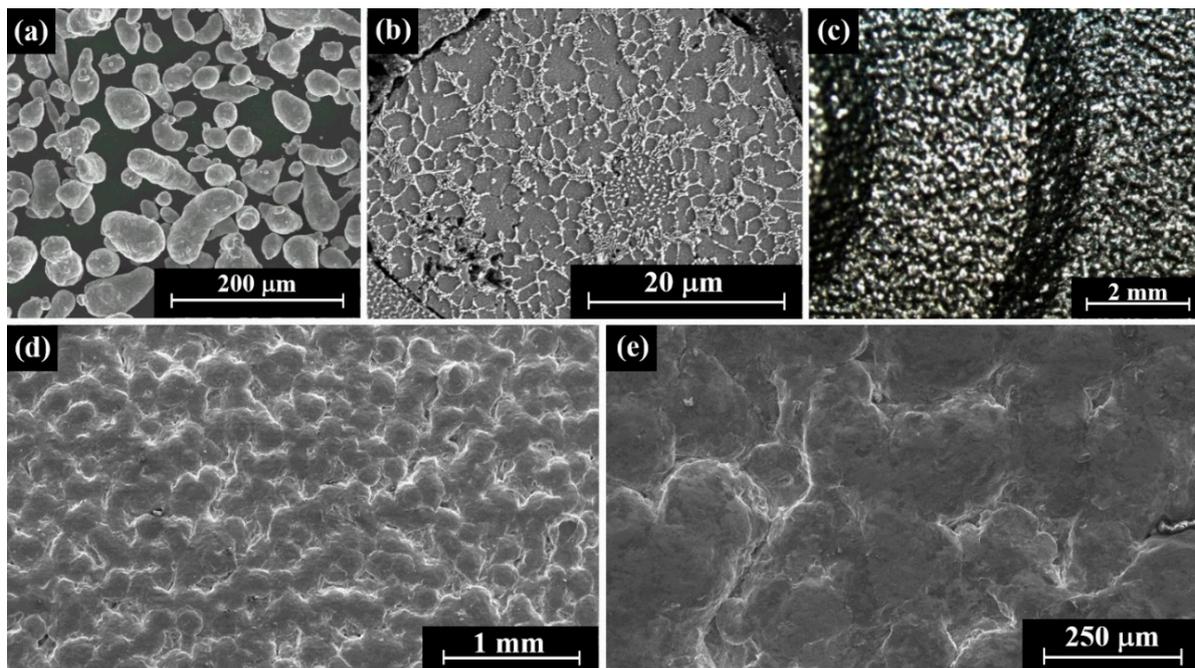
Figure 2. The representative surface of an as-printed AM-LPBF AlSi10Mg disk-shaped reference specimen (obverse): (**a**) AlSi10Mg feedstock, typical powder particles (SEM); (**b**) AlSi10Mg characteristic particle's cross-section; (**c**) a general view of the as-printed disk-shaped specimen (multi-focal light microscope); and (**d**,**e**) higher magnifications of the disk-shaped specimen surface (SEM).

2.2. Silver Electroless Plating on AM-LPBF AlSi10Mg

A silver electroless deposition bath (Figure 3, Table 2) was developed at Tel Aviv University (TAU) by Dresler et al. 2019 [42]. This electroless plating process was published earlier by Shacham-Diamand et al. 2000 [26]; however, it was never examined on the AlSi10Mg alloy or on any 3D-printed objects until 2019 [42]. The silver film was deposited by electroless plating on top of disk-shaped substrates covered with native oxide film (Figure 3a), according to the TAU process protocol [42]. The deposition process was applied at room temperature from an $AgNO_3$ base solution with hydrazine hydrate, N_2H_4, as the reducing agent that was totally oxidized due to the $N_2H_4 + 4OH^- - 4e \rightarrow N_2 + 4H_2O$ anodic reaction. Therefore, no hazardous products remained in the electrolyte after the silver deposition. Ammonia and acetic acid were used to complex the metal ions and to preserve the working pH in the range of 10.0−10.6, e.g., creating an ammonium–acetate buffer solution. This relatively stable bath was selected, since it yielded good quality silver coatings on many metal substrates without the need for brighteners [26].

Table 2. The electroless silver bath composition. Adapted with permission from [26,42]. Copyright 2020 Copyright IOPscience. Copyright 2019 Copyright Springer.

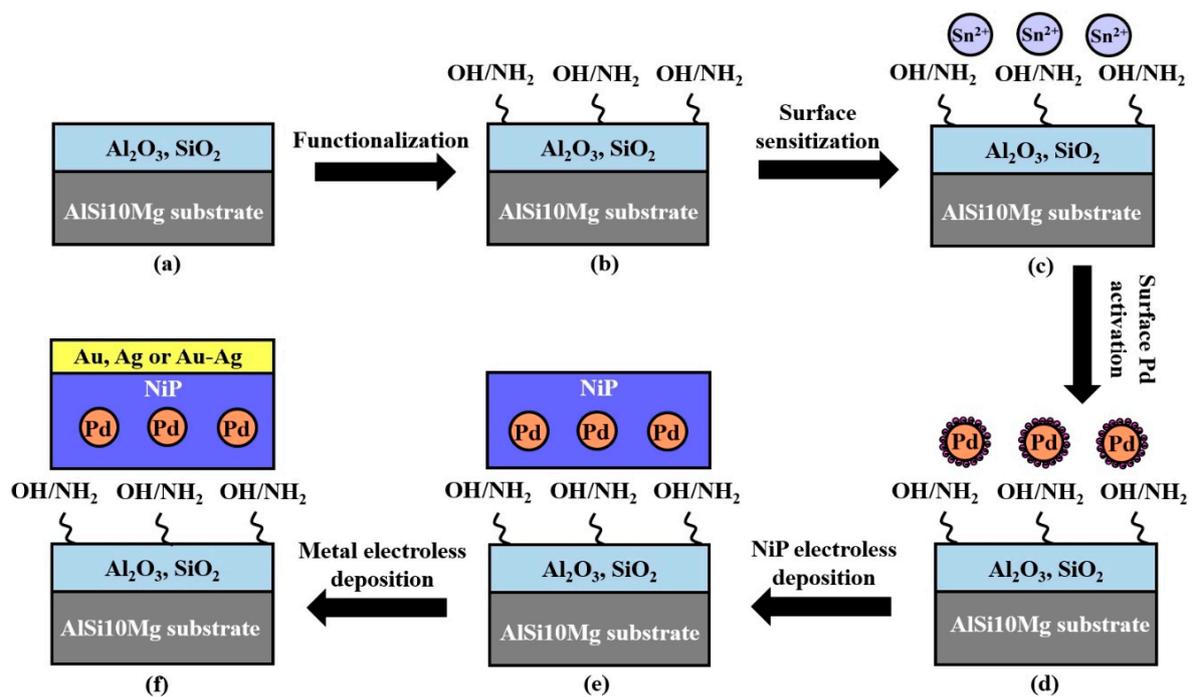| Component	Concentration (M)
Silver nitrate ($AgNO_3$)	0.03
Ammonia (NH_4OH)	1.0
Acetic acid (CH_3COOH)	0.5

Figure 3. Schematic illustration of the gold, silver, and electrum electroless plating process developed for the AM-LPBF AlSi10Mg surface coating: (**a**) The 3D-printed AlSi10Mg substrate covered with native oxide (Mg is not presented here since AlSi10Mg contains less than 0.5 wt.% Mg); (**b**) surface functionalization: sodium dodecyl sulfate (SDS)/silanization; (**c**) surface sensitization (optional), (**d**) surface Pd activation; (**e**) deposition of Ni–P interlayer (optional); and (**f**) electroless deposition of metal coating [42,43,48].

Before deposition, the surface of all AM-LPBF AlSi10Mg specimens (Figures 1d and 2c–e) was etched at room temperature for 1 min in a $NH_4F/HF/Ethylene$ glycol solution removing surface oxides. Next, six disk-shaped specimens were silver-plated by electroless deposition, while six more disk-shaped specimens were coated by an ultra-thin silane layer (e.g., "silanized") (functionalization step, Figure 3a,b). This "silanization" process was conducted at 70 °C for 3 h in 1% 3-aminopropyl-trimethoxysilane (TAPOS)/ethanol solution [21]. This process, also known as SAM, creates an ultra-thin stable, uniform, and transparent nano-scale thickness film, improving the adhesion of the Ag layer to the AlSi10Mg substrate. The SAM's molecules contain a functional group [52] and chemically bind to the 3D-printed surface [53], consequently yielding good adhesion [54] of the deposited electroless silver to the substrate. The surface of all twelve specimens was activated for 1 min in a Pd-citrate bath (pH 2) at room temperature (Figure 3c,d), forming metal catalytic seeds on the surface and initiating the electroless deposition process. The specimens were washed in deionized (DI) water after each step of the coating process (Figure 3). The silver was deposited for 3, 5, 7, and 10 min. After silver deposition, the coated samples were heated in an air-oven (MRC Laboratory Instruments, Holon, Israel) for 30 min at 110 °C [42].

A darkening process was applied to the silver coated disk-shaped specimens as well as to the silver coated 3D-printed coin replica specimens; this was done in order to emulate the appearance of ancient items. For that purpose, the coated samples were treated in saturated I_2/ethanol solution for 5 min at room temperature, and they were then washed in ethanol to eliminate unreacted iodine. Following the darkening process, the samples were air dried at room temperature and finally were polished with a flannel cloth [42].

This electroless silver plating bath and process were compared to a commercial 99.9 wt.% pure Ag coating (Interplate Ltd., Bnei Brak, Israel) produced from a semi-bright cyanide bath. The silver plating using the commercial bath was executed on a ≈9.3 μm nickel-phosphorus (Ni–P) interlayer containing 10 wt.% phosphorus. The commercial

processes ended with an air-oven heat treatment at 180 °C for 30 min. Limited information is presented here regarding the commercial electroless silver plating process due to commercial confidentiality [42].

2.3. Gold Electroless Plating on AM-LPBF AlSi10Mg

A laboratory-developed process for gold electroless deposition (Figure 3, Tables 3 and 4) was produced by Inberg et al. 2020 [43] at TAU. The coating was executed at 80–85 °C from a solution of a dicyanoaurate complex of gold and hypophosphite as a reducing agent (Table 4). This bath composition was already published by Krusenstern 1974 [55], yet it has never been applied on 3D-printed AlSi10Mg objects. Since the AlSi10Mg substrate is covered with native oxide film (Figure 3a), prior to the gold deposition, the surfaces of all the disk-shaped specimens were cleaned and etched. For this purpose, the specimens' surface was ultrasonically treated for 10 min at room temperature in a sodium dodecyl sulfate (SDS) solution (Figure 3b), and the weight of the specimens was reduced by about 0.001 g. The sensitization stage (Figure 3c) was performed at room temperature for 2 min, followed by palladium activation in a Pd-citrate bath [22] for 1 min (Figure 3d), which was performed also at room temperature. The Pd activation was done in order to generate catalytic seeds (nucleation sites) on the metal surface to initiate the ELD process. To improve the gold adhesion to the AlSi10Mg substrate and prevent pitting corrosion of the coating, the gold film was deposited on an interlayer of ≈1 μm nickel-phosphorus (≈5 wt.% P, Figure 3e). Ni–P plating was carried out at 95–96 °C for 1 h in the solution given in Table 3. The specimens were washed in DI water after each step and at the end of the process. Following the gold deposition (Figure 3f, Table 4), the specimens were heated in an air-oven at 110 °C for 30 min [43].

Table 3. The electroless Ni–P solution composition (pH = 4–6). Adapted with permission from [43]. Copyright 2020 Copyright Springer.

Component	Concentration (M)
Nickel(II) sulfate hexahydrate ($NiSO_4 \cdot 6H_2O$)	0.114
3-Na-citrate ($Na_3C_6H_5O_7$)	0.043
Sodium hypophosphite (NaH_2PO_2)	0.094
Sodium acetate ($NaCH_3COO$)	0.037

Table 4. Laboratory-developed electroless gold bath composition. Adapted with permission from [43]. Copyright 2020 Copyright Springer.

Component	Concentration (M)
Potassium dicyanoaurate [$KAu(CN)_2$]	0.007–0.010
Ammonium chloride (NH_4Cl)	1.3–1.4
3-Na-citrate ($Na_3C_6H_5O_7$)	0.155–0.170
Sodium hypophosphite (NaH_2PO_2)	0.075–0.094

The laboratory-developed coating was compared to a commercial coating process (Interplate Ltd., Bnei Brak, Israel) where the Au film was produced from a semi-bright cyanide bath. The commercial gold plating was executed on a ≈10 μm thick Ni–P (≈8 wt % P) interlayer. After the gold deposition, the coated samples were heated for 30 min in an air-oven at 180 °C. Only partial information is presented here regarding the commercial procedure due to commercial confidentiality [43].

2.4. Gold–Silver Electroless Plating on AM-LPBF AlSi10Mg

A process for electroless Au–Ag plating on 3D-printed disk-shaped specimens was developed by Inberg et al. 2020 (Figure 3) [48]. Prior to the deposition process, the oxide film (Figure 3a) that covered the AlSi10Mg surface was ultrasonically cleaned and etched for 10 min in a 12 g/L SDS solution at room temperature (Figure 3b). The quality of the

coating depends on the surface roughness, post-treatment of the AlSi10Mg substrate, and the cleaning process. The cleaning and etching steps reduced the weight of the 3D-printed specimens by about 0.001g. Next, a sensitization process was applied (Figure 3c) at room temperature for 2 min in a solution of $SnCl_2$/HCl (70 g/L of $SnCl_2$ and 40 mL/L of HCl). Palladium activation of the surface (Figure 3d) was done in a Pd-citrate solution for 1 min at room temperature to generate metal catalytic seeds that serve as nucleation sites. An Ni–P interlayer was deposited on the AlSi10Mg specimens (Figure 3e, Table 3) to improve the adhesion of the Au–Ag alloy to the substrate (Figure 3f). The electroless Au-Ag plating (Table 5) was performed at 80 and 90 °C and several times between 1.5 and 9 min. The specimens were washed in DI water after each step and at the end of the Au–Ag deposition process. Following the electrum deposition, the specimens were heated treated at 100 °C in an air-oven for 30–60 min [48].

Table 5. The laboratory-developed bath for Au-Ag electroless deposition (KOH, pH = 12), molar ratio [Ag]/[Au] in solution 1:2.

Component	Concentration (M)
Potassium dicyanoaurate [$KAu(CN)_2$]	0.007
Potassium silver cyanide [$KAg(CN)_2$]	0.0035
3-Na-citrate ($Na_3C_6H_5O_7$)	0.170
Hydrazine hydrate (H_6N_2O)	0.015
Polyethylene glycol 1500 (PEG 1500)	0.0003
Sodium saccharin ($C_7H_4NNaO_3S$)	0.002

2.5. Characterization Methods

The following characterization procedures and tests were applied to the AM-LPBF 3D-printed AlSi10Mg disk-shaped specimens before and after Ag, Au, and electrum coating:

(a) The specimens were weighed in their as-printed condition, after cleaning, after etching, after coating by Ni–P interlayer, and after the final coating. The measurements were made with an analytical MRC ASB-220-C2 balance (MRC Laboratory Instruments, Holon, Israel) with a precision of ±0.0001 g [42,48].

(b) A qualitative pilling test was performed on all coated specimens with transparent vinyl tape in order to evaluate the adhesion of the metal coatings to the printed substrate [42].

(c) The thickness of the Ni–P interlayer and the electroless deposited Au, Ag, and Au-Ag films was measured by a calibrated high-resolution FISCHERSCOPE X-RAY XDL 230 X-ray fluorescence (XRF) instrument (Fischer Technology, Inc., Windsor, CT, USA), with an approximation error of ±0.1 μm [42]. Each measurement was performed in a circle of ≈1 mm in diameter for 30 s.

(d) Average roughness (Ra) and root mean square (RMS) roughness measurements were accomplished with Alpha-Step D-500 Stylus profilometer (KLA Corporation, Milpitas, CA, USA), with vertical high-resolution profiling of 0.1 nm. The average surface roughness was calculated considering seven to 10 measurements [42].

(e) X-ray diffraction (XRD) analysis was performed before and after electroless coating with a powder PANalytical Empyrean X-Ray Diffractometer (Malvern Panalytical Company, Malvern, UK) to determine the crystal structure and lattice constants of the coated layers. Data were collected in the common symmetrical Bragg–Brentano geometry (θ/θ) using a Cu Kα radiation (wavelength of λ = 1.541 Å) operating at 40 kV and 30 mA. Phase identification from the XRD results was done by using International Centre for Diffraction Data (ICDD) databases and Pearson's handbook with the assistance of a PowderCell program for powder pattern calculation [48,56].

(f) HIROX RH-2000 digital 3D multi-focal light microscope (LM) (HIROX Company, Tokyo, Japan), equipped with different optical lenses, a high-intensity LED lighting source, and powerful 3D software, was used to characterize the specimens' general

surface quality before and after coating and to identify microscopic discontinuities and defects [43,57].

(g)　Scanning electron microscopy (SEM) observation and energy-dispersive spectroscopy (EDS) analysis were performed with an ESEM FEI Quanta 200 FEG instrument (FEI Company, Hillsboro, OR, USA) in the high vacuum mode, before and after the electroless coating. An Everhart–Thonley secondary electron liquid-nitrogen-cooled Si(Li) X-ray EDS detector (Oxford Instruments Company, Abingdon, UK), calibrated with standard specimens received from the instrument manufacturer, was utilized to measure the chemical composition of the substrate and the coating. The EDS analysis provided results with an estimated error of 1% [42].

(h)　Focused ion beam (FIB) technology with an accelerated high-energy gallium ions source, equipped with high-resolution SEM Helios 600 SEM/FIB dual beam (Thermo Fisher Scientific, Waltham, MA, USA), was applied in order to observe the cross-section of the silver, gold, and electrum plated specimens. Before digging into the specimen, a thin layer of platinum was deposited (voltage of 2.0 kV and current of 2.7 nA) on the surface of the samples to protect the deposited films during the milling processes. The digging was performed with a high voltage of 30.0 kV and a beam current of 21.0 nA, which was followed by etching with a 6.5 nA beam current. The FIB's milled cut dimensions were 15 μm × 15 μm, with a depth of ≈7 μm [42].

(i)　X-ray photoelectron spectroscopy (XPS) profiling with an Al Kα monochromatic irradiation source (1486.6 eV) was performed to the electrum coated specimens by using 5600 Multi-Technique System (PHI Inc., Chanhassen, MN, USA) in an ultra-high vacuum (UHV) with a base pressure of 2.5×10^{-10} Torr. The specimens were not charged during the analysis. The outcome electrons were examined with a Spherical Capacitor Analyzer (SCA), using a 0.8 mm slit aperture. The sputtering was performed with a 4kV Ar$^+$ Ion Gun using 17 Å/min sputter rate on SiO_2/Si and was assumed to be approximately three times higher on Au–Ag [48].

3. Results

3.1. AM-LPBF AlSi10Mg Disk-Shaped Specimens

The disk-shaped specimens and the coin replica specimens revealed rough and slightly porous surfaces (Figure 4a–c), as expected for vertical AM-LPBF AlSi10Mg surfaces [9,12,58]. The measured mass values of the AM-LPBF AlSi10Mg disk-shaped specimens were between 4.817 and 4.859 g, with diameter values lying between 25.90 and 26.07 mm. The as-printed surface roughness of the specimens was 21.23 μm according to RMS and 17.03 μm according to Ra measurements [42].

LM and SEM observation of the specimens revealed a rough surface morphology (Figure 2c–e). SEM-EDS analysis revealed that the AlSi10Mg disk-shaped specimens were composed of aluminum, containing 9.8 wt.%−11.3 wt.% Si, ≈2.3 wt.% O, and 0.4 wt.%−0.5 wt.% Mg [42].

The XRD analysis of the AlSi10Mg samples (Figure 5a) exhibited the characteristic peaks of Al and Si (Al–Si eutectic structure), yet since the content of Mg is relatively low (less than 0.5 wt.%), Mg or its compound peaks were not detected [42].
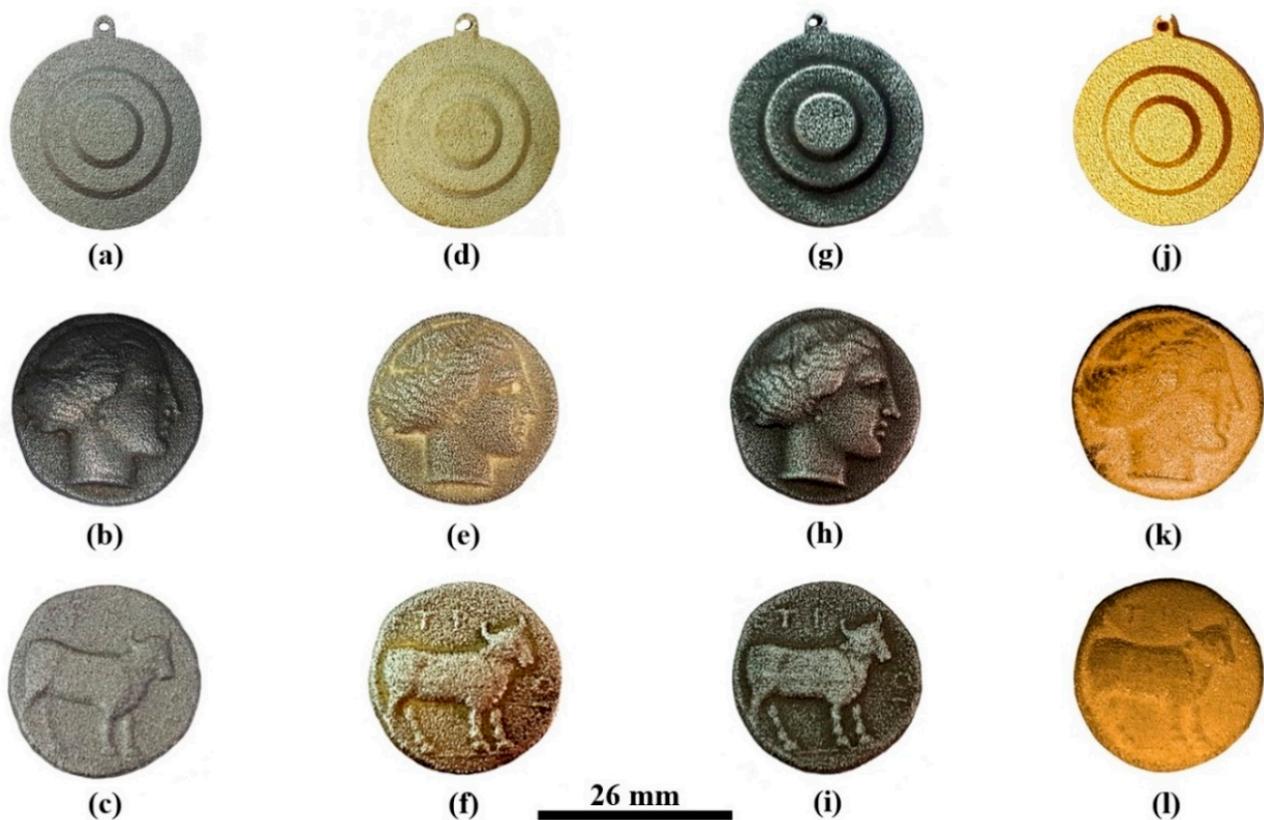
Figure 4. The experimental specimens before and after coating: (**a**) the as-printed AM-LPBF AlSi10Mg disk-shaped reference; (**b**,**c**) the as-printed AM-LPBF AlSi10Mg coin replica (obverse and reverse, respectively); (**d**) the as-printed disk-shaped specimen coated with Ag; (**e**,**f**) the coin replica coated with Ag; (**g**) the disk specimen coated with Ag after darkening process; (**h**,**i**) the coin replica coated with Ag after darkening process; (**j**) the disk-shaped specimen coated with Au; and (**k**,**l**) the coin replica coated with Au.

3.2. Silver Electroless Plating on AM-LPBF AlSi10Mg Disk-Shaped Specimens

The disk-shaped and coin replica specimens coated with the laboratory-developed silver film exhibited a relatively uniform bright but not shiny surface, with rough topography (Figure 4d–f). Yet the surface of the silver coated samples was less rough than the bare surface. The measured mass values of the silver coated specimens were between 4.838 and 4.890 g. The mass of the silver deposited layer was measured to be 0.002 g for the 3 min coating and 0.066 g for the 10 min coating. The qualitative pilling test examination of the silver-coated samples (with and without SAM) revealed a high-quality coating. A satisfactory appearance of authentic ancient objects was achieved for both silver-coated disk-shaped and coin replica specimens after the darkening process (Figure 4g–i) [42].

The XRD analysis of the silver-coated surface (Figure 5b, Graph 1) revealed characteristic peaks of the Ag, Al, and Si, as expected of the AlSi10Mg surface coated with ≈1 μm silver film. The presence of characteristic peaks of aluminum and silicon probably results from the existence of voids and cavities in the silver film [42].

The thickness of the silver coating with silanization treatment was 1.06 ± 0.12 μm and without silanization was 1.16 ± 0.16 μm (XRF results, Figure 6a). The average RMS and Ra surface roughness values (measured by profilometer) were both reduced after coating (Figure 6b). The SAM layer had no noteworthy effect on the Ag layer deposition rate allowed by the Pd–Ag binding energy [23,42]. SEM observation of the coated surface revealed a rough surface morphology (Figure 7a,b). The roughness values were reduced when the deposition time was increased (Figure 6b).
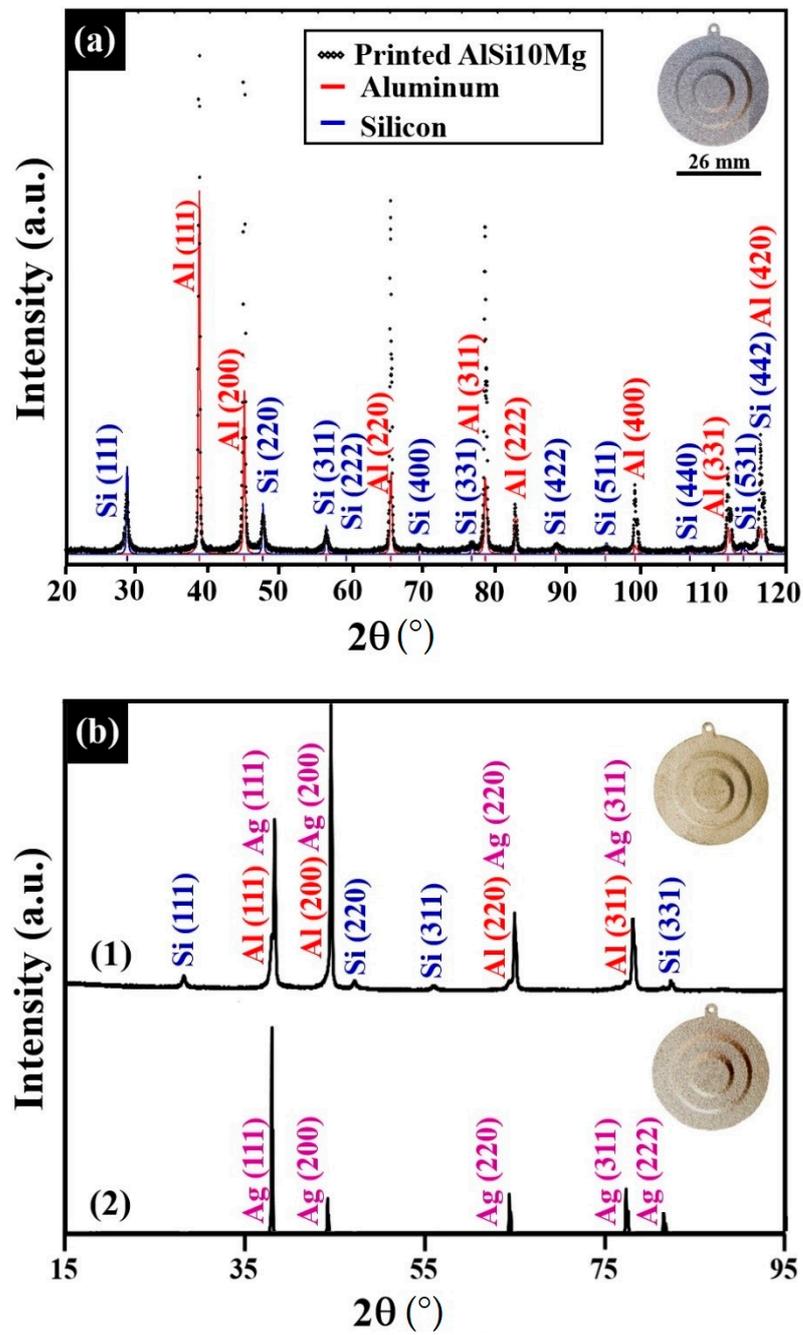
Figure 5. XRD patterns of the: (**a**) as-printed AM-LPBF AlSi10Mg substrate; (**b**) AlSi10Mg disk-shaped specimens coated with laboratory-developed silver (Ag thickness of ≈1 μm, Graph 1) and commercial coating (Ag thickness ≈16 μm, Graph 2).
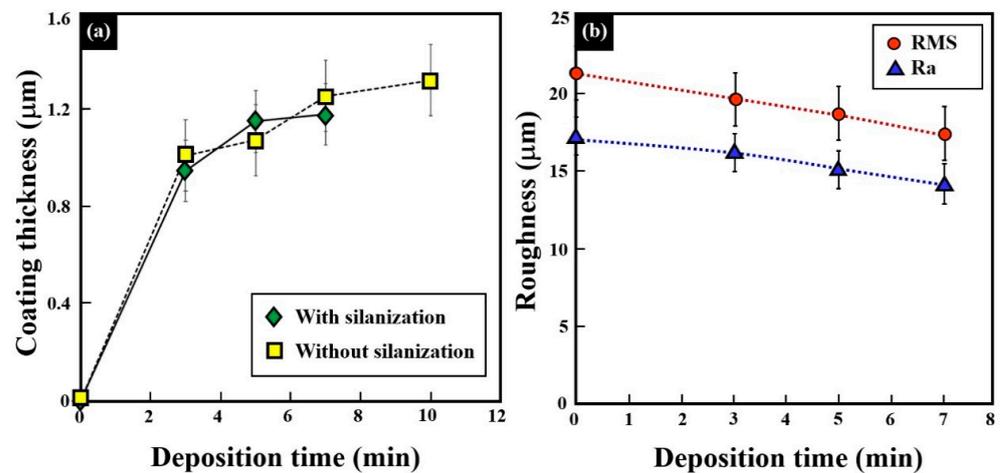
Figure 6. The laboratory-developed silver coating on top of AM-LPBF AlSi10Mg substrate: (**a**) film thickness as a function of deposition time with and without silanization; and (**b**) RMS and Ra surface roughness without silanization (measured by profilometer).

SEM-EDS analysis of the coated disk-shaped specimens revealed that the silver layer contains up to 2.1 wt.% O, up to 1.8 wt.% C, and 0.7 wt.% Al. FIB-SEM examination of the 3 min silver coated specimen's cross-section (Figure 8a,b), revealed that the silver layer thickness varies between 0.5 and 1.0 μm. The silver film showed a wavy topography behavior with some grooves, which were caused by the high roughness of the AlSi10Mg substrate and the absence of an Ni–P interlayer [42].
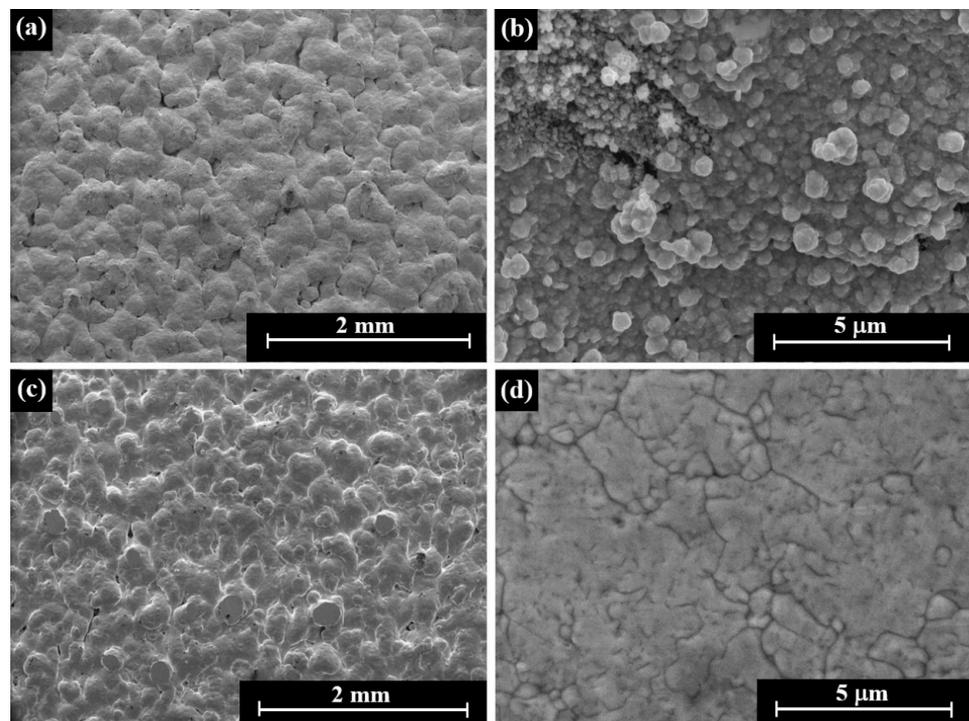
Figure 7. SEM images of the AM-LPBF AlSi10Mg disk-shaped specimens after silver electroless plating: (**a**,**b**) the external surface of the laboratory-developed Ag coated specimen; and (**c**,**d**) the external surface of the commercial Ag coated specimen.

The commercial silver-coated disk-shaped specimens exhibited uniform shiny metal surfaces with rough topography; however, the coated surface roughness was smaller than that of the as-printed surface. The qualitative pilling test of the commercial silver coating

also confirmed good adhesion. The measured thickness (using the XRF technique) of the commercial coating was between 14.80 and 17.00 μm. The XRD analysis of the commercial silver film showed characteristic peaks of the Ag (Figure 5b, Graph 2). SEM examination of the coated specimens revealed a surface morphology practically similar to the amorphous materials (Figure 7c,d). EDS analysis of the commercial coating shows that it was composed of 100 wt.% Ag [42].

3.3. Gold Electroless Plating on AM-LPBF AlSi10Mg Disk-Shaped Specimens

The disk-shaped specimens and the coin replica specimens coated with the laboratory-developed gold film revealed uniform bright and shiny surfaces, with rough topography (Figure 4j–l). Yet the surface of the coated specimens was slightly less rough than the uncoated surface [43].

The XRD analysis of the laboratory-developed specimen (Figure 9a) revealed that it was composed of crystalline Au and partially quasi-amorphous Ni. Characteristic peaks of the Al and Si were also detected [43].
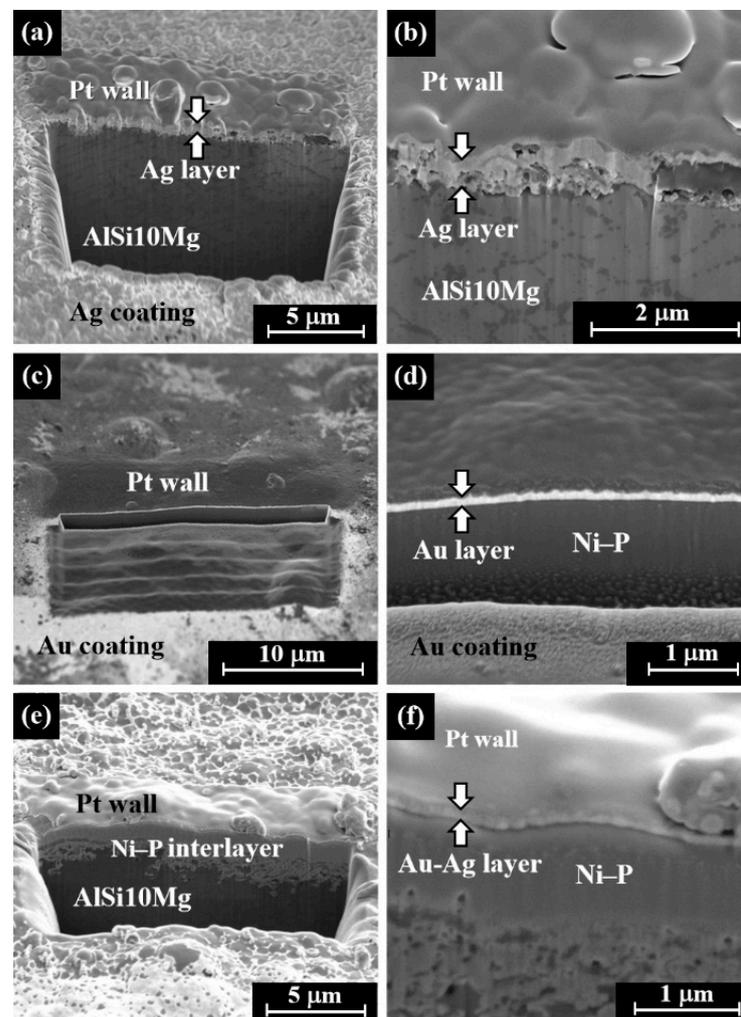
Figure 8. SEM images of the laboratory-plated AlSi10Mg sample following selective material milling by the focused ion beam (FIB) technology starting from the specimen surface: (**a,b**) cross-section of the Ag-plated sample, showing the hole cut by FIB, the Pt wall behind the hole, and the printed substrate with the Ag layer on top; (**c,d**) a cross-section of the Au-plated sample, showing the hole cut by FIB, the Pt wall, the substrate, the ≈1 μm Ni–P (≈5 wt.% P) layer, and the Au layer on top (white layer); (**e,f**) cross-section of the electrum-plated sample, showing the hole cut by FIB, the Pt wall, the substrate, the Ni–P layer, and the Au–Ag layer on top.
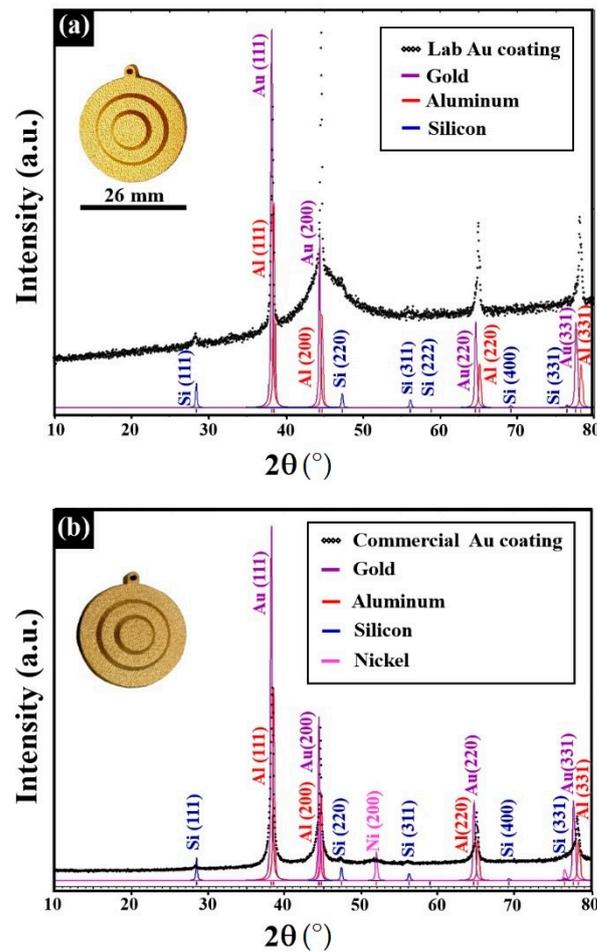
Figure 9. XRD patterns of the AlSi10Mg printed disk-shaped specimens electroless gold plated, the dark line represents the current experimental results: (**a**) laboratory-developed Au coating and (**b**) commercial Au-plated coating.

The thickness of the Au film according to the XRF measurements was 0.07 μm for the 3 min deposition and 0.70 μm for the 10 min deposition (Figure 10a). The mass values of the coated specimens including the Ni–P and gold layers were between 4.888 and 4.939 g. The mass of the deposited gold layer was 0.024 g for the 1 min coating and 0.079 g for the 5 min coating. The average RMS and Ra surface roughness were both slightly reduced after the coating process (Figure 10b), which may be attributed to the Ni–P interlayer (with thickness of 1 μm). Moreover, the roughness values monotonically decrease with deposition time (Figure 10b). Nevertheless, it is important to note that the thickness of the Ni–P interlayer and the gold film are both well below the average surface roughness. Therefore, the surface appearance of the AM-LPBF AlSi10Mg substrate on the macroscopic level is quite close to that of the laboratory-developed Au coated specimens (Figure 11a,b) [43].
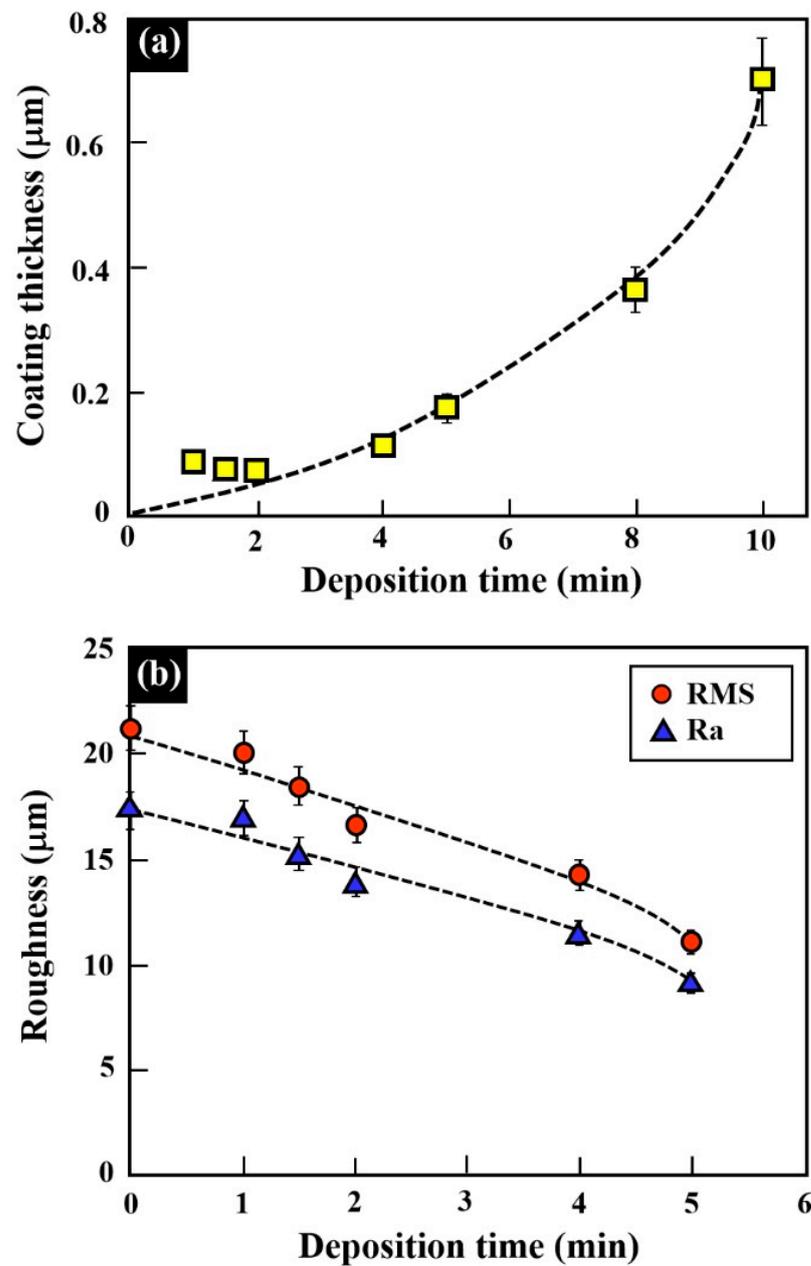
Figure 10. The gold coating on top of AM-LPBF AlSi10Mg printed substrate: (**a**) film thickness as the function of time; and (**b**) the RMS and Ra roughness (measured by profilometer).

The deposited gold was too thin to allow the use of conventional metallographic cross-section methods. Therefore, a cross-section was created by FIB technology, enabling FIB-SEM examination of a 5 min gold coated specimen (Figure 8c,d). A relatively uniform film of gold coating was observed, with thickness varying between 0.09 and 0.13 μm. At the microscopic level, this uniform gold film does not follow the wavy topography of the AM-LPBF AlSi10Mg substrate. The AM-LPBF AlSi10Mg surface roughness was relatively reduced by the addition of the Ni–P interlayer as expected [32]. The FIB-SEM thickness measurements were in good agreement with the XRF technique measurements. For instance, the XRF measurements of the 5 min gold deposited specimen gave a measured film thickness of 0.17 μm [43].
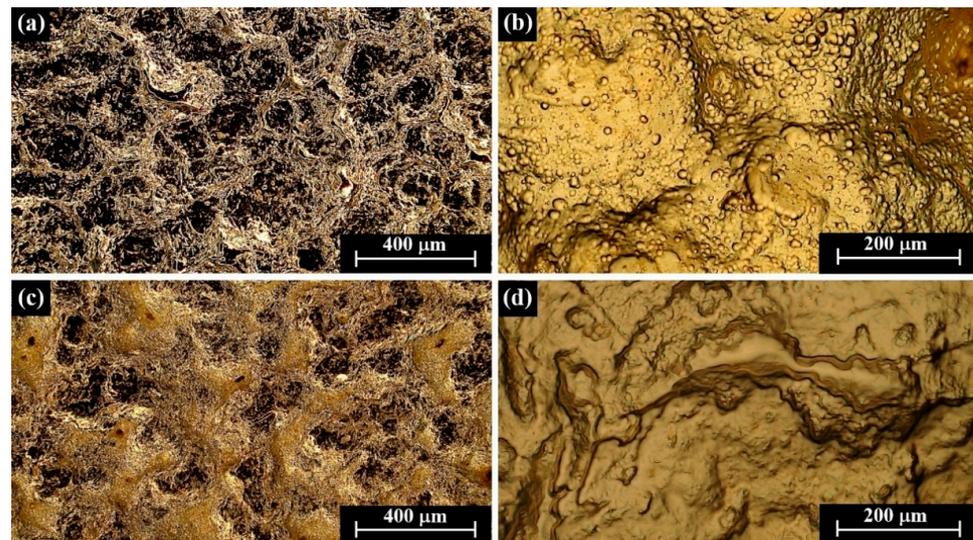
Figure 11. Multi-focal optical light microscope (LM) images of the AM-LPBF AlSi10Mg disk-shaped specimens: (**a**,**b**) laboratory-developed Au coating; and (**c**,**d**) commercial Au coating.

The commercial gold coated disk-shaped specimens displayed relatively uniform shiny metal surfaces with rough topography (Figure 11a,b). Yet the coated surface was less rough than the AM-LPBF AlSi10Mg surface. The qualitative pilling test of the commercial gold film also shows good adhesion. The measured thickness of the commercial coating was 0.50 ± 0.02 µm according to XRF measurements. The XRD analysis of the commercial gold film revealed that the coated surface is composed of crystalline Au and nanocrystalline Ni–P (Figure 9b). Asymmetric peak profiles were observed by Inberg et al. 2020, owing to overlapping of Au and Al Bragg reflections. Naturally, beneath the coatings, the substrate was composed of Al and Si crystalline phases [43].

3.4. Gold–Silver Electroless Plating on AM-LPBF AlSi10Mg Disk-Shaped Specimens

Based on the visual testing examination, the Au-Ag coated AM-LPBF AlSi10Mg disk-shaped specimens exhibited uniform shiny metal surfaces with rough topography (Figures 12 and 13). Yet the Au–Ag coated specimens were somewhat less rough than the uncoated ones. It is noteworthy that the specimens deposited with 1:1 Ag/Au molar ratio of solution (Figure 12b–d) and 1:2 Ag/Au molar ratio of solution at 80 °C (Figure 12e–h) display a shiny gray–silver color coating. Yet specimens produced with 1:2 Ag/Au molar ratio of solution at 90 °C (Figure 12i–l) exhibited a shiny yellow–gold color coating. The qualitative pilling test of the Au-Ag coated specimens revealed high-quality adhesion [48]. LM examinations of the electrum coated specimens exposed rough topography, but it was slightly less than that of the as-printed surface, with rather uniform shiny metal surfaces (Figure 13), whereas the films deposited at 80 °C were shiny gray–silver with a slight yellow tone (Figure 13c–f), and the film deposited at 90 °C was shiny yellow–gold (Figure 13g,h).
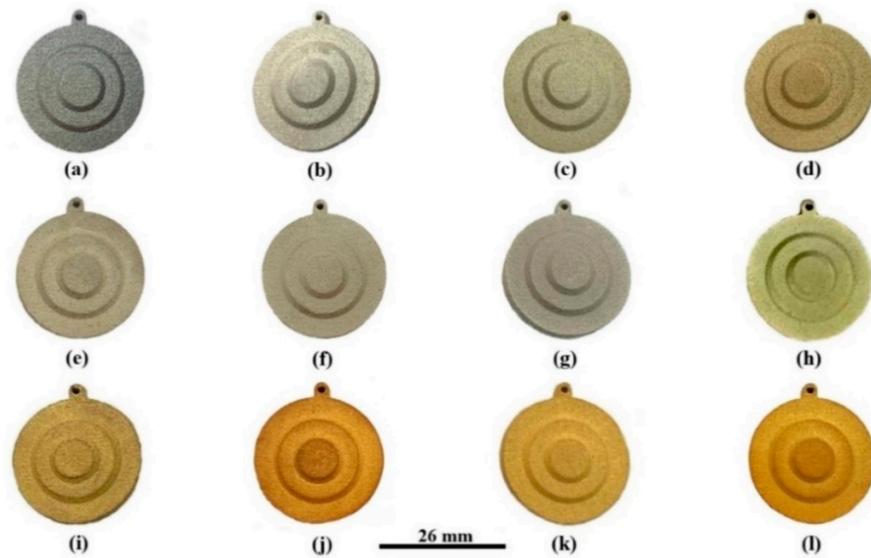
Figure 12. The AM-LPBF AlSi10Mg disk-shaped specimens, coated with electroless Au–Ag film: (**a**) as-printed reference specimen; (**b–d**) specimens coated with 1:1 Ag/Au molar ratio of solution at 80 °C; (**e–h**) coated with 1:2 Ag/Au molar ratio of solution at 80 °C; and (**i–l**) specimens coated with 1:2 Ag/Au molar ratio at 90 °C.
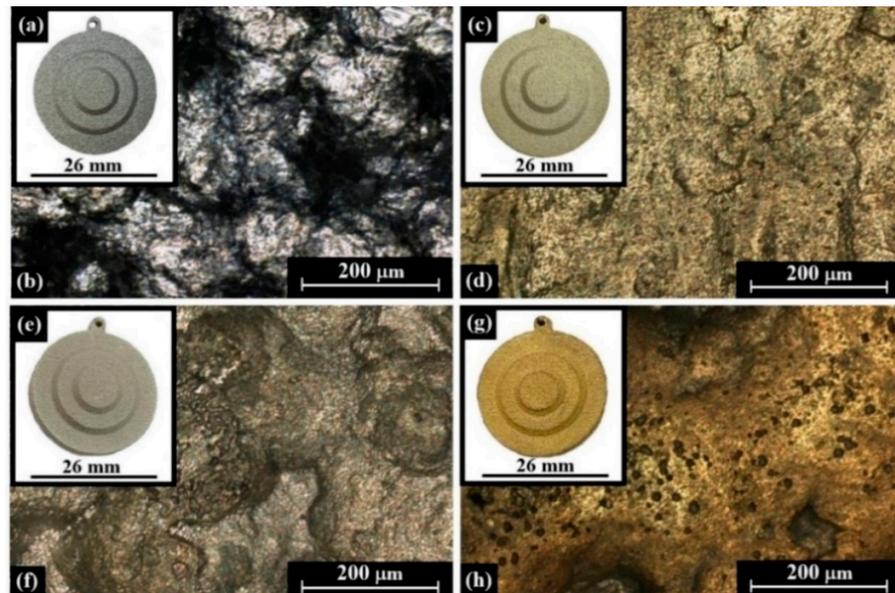

Figure 13. Optical images of the AM-LPBF AlSi10Mg disk-shaped specimens' surface: (**a,b**) as-printed sample; (**c,d**) covered with electroless electrum layer, produced with 1:1 Ag/Au molar ratio of solution at 80 °C; (**e,f**) covered with electroless electrum layer, produced with 1:2 Ag/Au molar ratio of solution at 80 °C; and (**g,h**) covered with electroless electrum layer, produced with 1:2 Ag/Au molar ratio of solution at 90 °C.

The XRD analysis results of the laboratory-developed electrum coatings revealed that they were composed of an Au-Ag crystalline solid-solution phase, with lattice parameter between 4.076 ± 0.001 Å and 4.080 ± 0.001 Å, depending on molar ratio of the metals in the solution and the temperature of the coating process; underneath the Au–Ag film, a quasi-amorphous or a mixed quasi-amorphous and nanocrystalline Ni–P interlayer (Figure 14, Table 6) was found. It should be noted that the Ni–P interlayer of the samples deposited at 80 °C displays a disordered atomic-scale quasi-amorphous structure, whereas the interlayer on samples deposited at 90 °C exhibits a mix of a quasi-amorphous and a nanocrystalline

structure. Since the deposition process was performed below 100 °C, the crystallization around nucleation centers occurred at a low rate, allowing the growth of quasi-amorphous or mixed Ni–P phases [48].
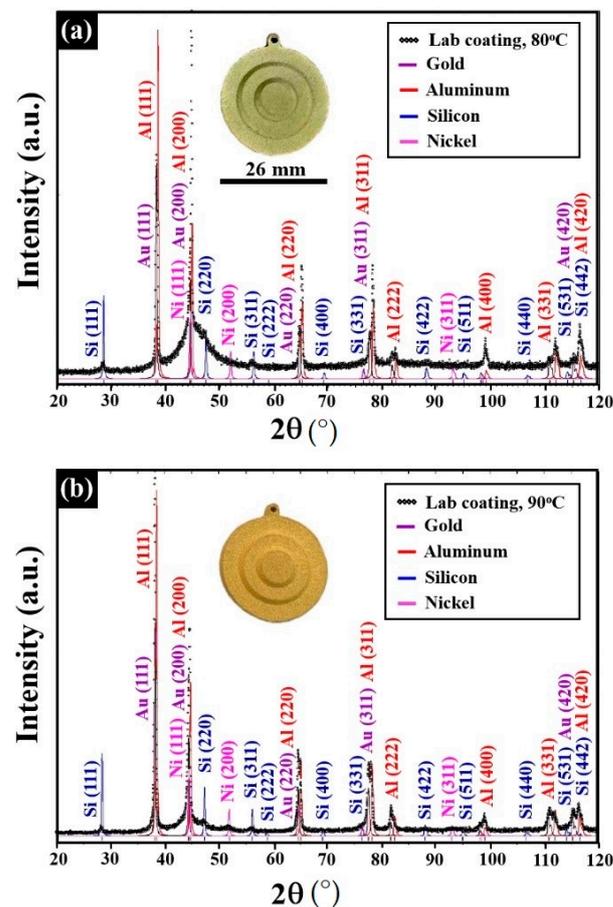

Figure 14. XRD patterns of the AlSi10Mg disk-shaped specimens electrum-plated with laboratory-developed electroless coating; the dark line represents the current experimental results: (**a**) produced with 1:2 Ag/Au molar ratio of solution at 80 °C; and (**b**) produced with 1:2 Ag/Au molar ratio of solution at 90 °C.

Table 6. Phase identification and electrum lattice parameter for the Au-Ag coated specimens.

Specimen	Lattice Parameter (Å)	Characteristics of the Au–Ag Coating	Characteristics of the Ni–P Interlayer	Characteristics of the Substrate
1:1 Ag/Au molar ratio at 80 °C	4.080 (±0.001)	Rich in Ag, solid-solution crystalline phase	Quasi-amorphous	Major crystalline phase Al Minor crystalline phase Si
1:2 Ag/Au molar ratio at 80 °C	4.079 (±0.001)			
1:2 Ag/Au molar ratio at 90 °C	4.076 (±0.001)	Rich in Au, solid-solution crystalline phase	Mix of quasi-amorphous and nanocrystalline	

The total mass values of the Ni–P interlayer and the electrum deposited films were between 0.012 and 0.044 g. The mass of the Au-Ag films increases substantially during the first 3–4 min of the deposition process (Figure 15a). A very thin Au-Ag film, with thickness up to 0.363 µm, was measured by an XRF instrument (Figure 15b). The measured thickness of the Ni–P interlayer was between 2.3 and 5.7 µm [48].
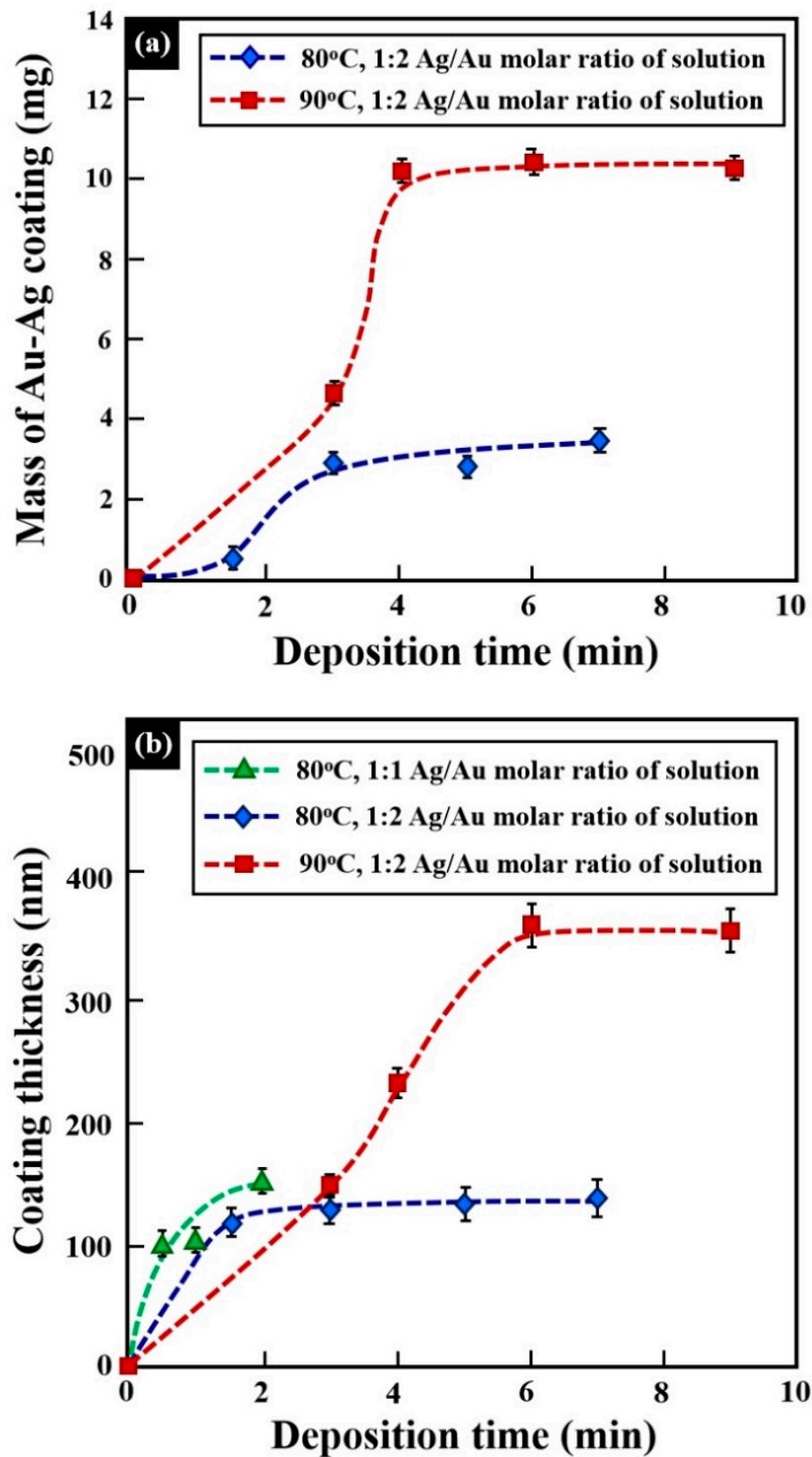
Figure 15. Laboratory-developed electrum (Au–Ag) coatings deposited at 80 and 90 °C: (**a**) mass of the coating after eliminating the Ni–P interlayer contribution vs. deposition time; and (**b**) thickness of the coating film (measured by X-ray fluorescence instrument) vs. deposition time.

The RMS and Ra surface roughness values of the Au–Ag coated specimens were somewhat lower than the roughness of as received AM-LPBF AlSi10Mg surface (Figure 16). This may be explained by the surface smoothing of the as-printed surface by the Ni–P interlayer. Moreover, when the deposition time was increased, the RMS and Ra roughness values were reduced (Figure 16) [48].
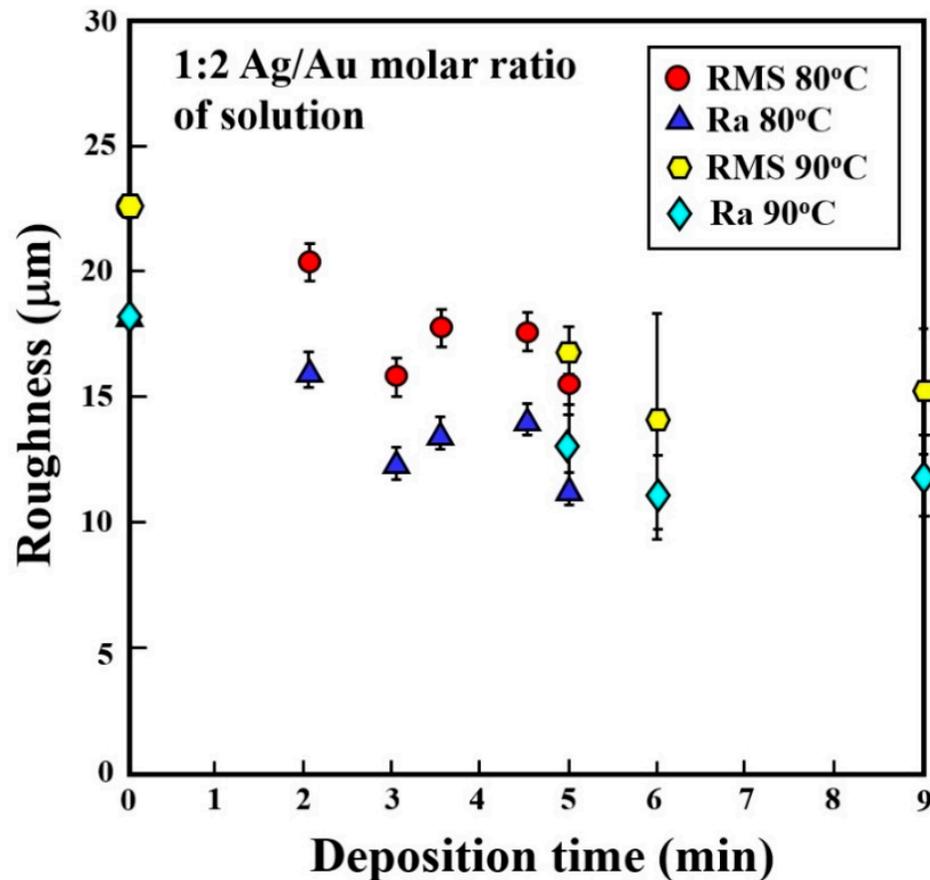
Figure 16. The root mean square (RMS) and roughness (Ra) roughness of the AM-LPBF AlSi10Mg disk-shaped specimens coated with electrum film (measured by profilometer) vs. deposition time.

The Au–Ag coating deposited from a solution with 1:1 Ag/Au molar ratio at 80 °C was characterized by the FIB-SEM technique (Figure 8e–f). The relatively uniform electrum film was achieved due to the Ni–P interlayer, with average Au-Ag thickness of ≈0.1 μm [48].

Based on the XPS profile analysis (Figure 17), the thickness of the Au-Ag layer after 3 min deposition at 80 and 90 °C was ≈0.1 and 0.25 μm, respectively. For electrum deposition from a 1:2 Ag/Au molar ratio solution, silver was dominant at 80 °C in Au–Ag film, at the beginning of the deposition process and at 90 °C, gold was first identified on the interface [48].
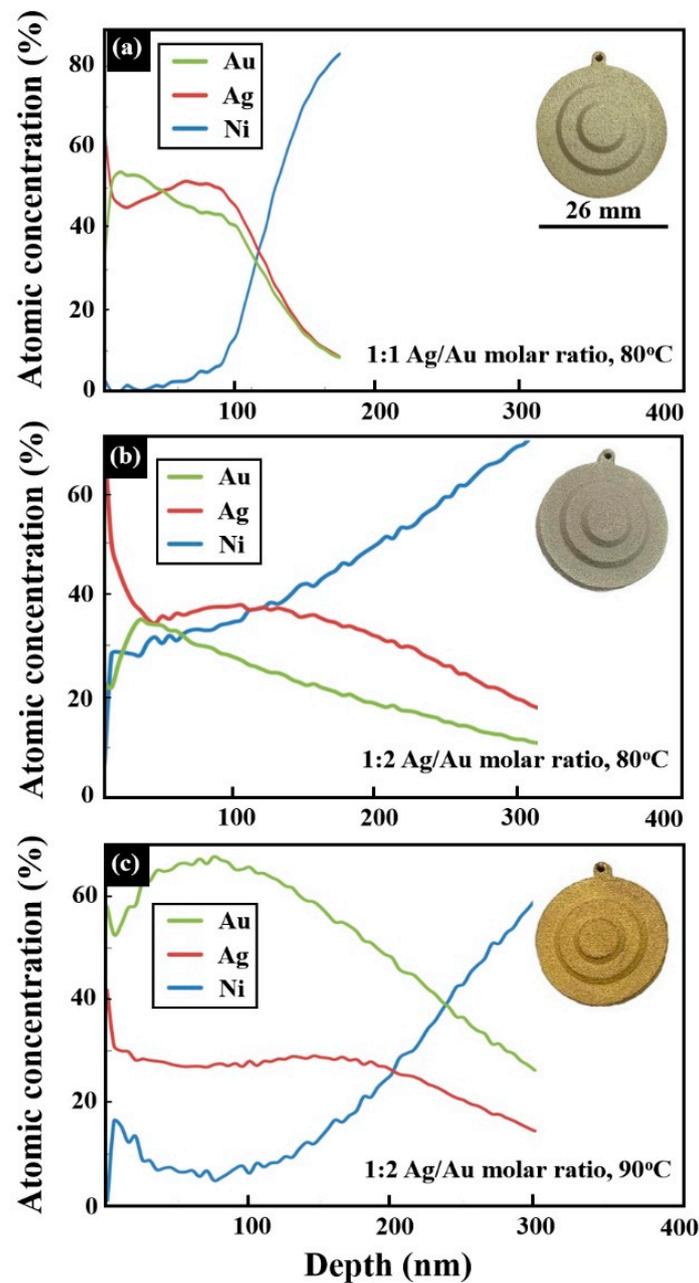
Figure 17. XPS elemental analysis profiles of the Au–Ag film coated on the disk-shaped specimen: (**a**) deposition made with 1:1 Ag/Au molar ratio in solution at 80 °C; (**b**) deposition made with 1:2 Ag/Au molar ratio in solution at 80 °C; and (**c**) deposition made with 1:2 Ag/Au molar ratio in solution at 90 °C.

4. Discussion

AM-LPBF technology has great potential for various industrial applications, among them electronics, aerospace, biomedical, heat exchangers, lightweight structures [59], and electric motors [60]. In some AM-LPBF objects, additional post-printing surface modification is needed to improve surface properties.

The current review has been done based on information available in the literature (the last search was done in March 2021) and as a part of an ongoing study performed by the authors [42,43,48]. The objective of this study was to review a novel laboratory-developed environmental-friendly and low-cost surface finishing process of AM-LPBF AlSi10Mg parts by electroless deposition of gold, silver, and gold-silver alloys, and to propose a methodology suitable for an effective metallization process. For that purpose,

an introduction is presented, reviewing the manufacturing technology of 3D printing of AlSi10Mg parts by AM-LPBF technology. Next, a literature survey is presented concerning the ELD process of gold, silver, and Au–Ag alloys. In the materials and experimental methods part, the fabrication process of AM-LPBF AlSi10Mg specimens is described, including the printing parameters and the chemical composition of the AlSi10Mg powder. Next, the electroless plating processes of Ag, Au, and Au–Ag alloy on top of AM-LPBF AlSi10Mg specimens is described, and the specific bath composition of each coating process is presented. In addition, the characterization methods of Dresler et al. 2019 [42] and Inberg et al. 2020 [43,48] are presented, while displaying the parameters of each method. In the results part, the final Ag [42], Au [43], and Au-Ag [48] ELD coatings on top of the AM-LPBF AlSi10Mg disk-shaped specimens and their characterization analyses results are presented. This part includes weighed and thickness measurements, qualitative pilling test results, thickness measurements of the Ag, Au, Au–Ag deposited films, and of the Ni–P interlayer, measurements of Ra and RMS roughness values before and after coating, XRD analysis results of the coatings, 3D multi-focal LM, SEM, and FIB-SEM observations of the specimens' surface and their cross-section, and XPS elemental depth profile analysis. Lastly, in the discussion part, the results of the examined Ag, Au, and Au–Ag ELD films are compared and discussed, and a methodology is suggested.

The Ag, Au, and Au–Ag ELD coatings were chosen based on their esthetic appearance, good corrosion resistance, and their excellent electrical and thermal conductivity. In the case of the electroless silver plating, the thickness of the Ag film grew significantly and linearly during the first 3 min of the deposition process; then, the thickness growth started to slow down until film thickness saturation was reached (Figure 6a). In the case of the electroless gold plating, at the beginning of the process, the gold deposition rate was lower than the silver deposition rate. Although an acceleration in the Au deposition rate occurred, the coating thickness did not reach saturation (Figure 10a). In the electrum deposition process, the kinetics were similar to the silver deposition process; hence, thickness growth started to slow down with time until saturation of the film thickness was accomplished (Figure 15b).

Only a small reduction of the surface roughness compared to the as-printed AlSi10Mg substrate was observed in all laboratory-developed electroless deposition processes. This may be explained by the thinness of the metal covering of the very rough as-printed LPBF surface. The surface roughness values of the laboratory-developed Ag, Au, and Au–Ag coatings were marginally reduced after plating (Figure 6b, Figure 10b, and Figure 16, respectively). Despite the kinetic differences observed in the deposition rate and thickness growth of the Ag, Au, and Au–Ag films (Figure 6a, Figure 10a, and Figure 15b, respectively), the decrease in roughness due to the increase in the thickness of the coating is similar for all coated metals (Figures 6b, 10b and 16, respectively); i.e., the roughness decreases as the deposition time increases.

All the laboratory-developed Ag, Au, and Au–Ag films showed a relatively uniform bright surface at the macroscopic level, exhibiting a rather rough topography. At the microscopic level of the laboratory-developed silver and gold deposits, small grains (a range of a few tens to a few hundreds of nanometers) were observed by SEM and multifocal LM (Figures 7b and 11b). According to Duhin et al. 2011, the presence of such a tiny grain structure is the result of the usage of nanometric-scale Pd particles, which serve as nucleation sites during the deposition process [61]. Phase identification of the Au, Ag, and electrum-coated specimens by XRD analysis revealed that the coatings were composed of crystalline phases [42,43,48]. The microstructure of the commercial Ag and Au coatings is slightly different, with a smoother macrostructure appearance (Figures 7d and 11c). This is due to the use of different manufacturing processes, including bath composition, applied interlayer, and post-deposition heat treatment [42,43]. Elevated temperature heat treatment allows grains to coalescence quickly due to a higher driving force, leading to smoother macrostructures [44,62].

FIB-SEM examination of the 3 min silver-coated specimen cross-section (Figure 8a,b) revealed a non-uniform silver film; the thickness varies between 0.5 and 1.0 μm, following the rough wavy topography of the as-printed AlSi10Mg substrate [42]. Relatively uniform gold and electrum films were attained due to the presence of Ni–P interlayer (Figure 8c,d) [43], with an average thickness of ≈0.1 μm.

Based on the XPS profile analysis of the 1:2 Ag/Au molar ratio in solution, the thickness of the electrum layer after 3 min of deposition time from a solution with 1:2 Ag/Au molar ratio was ≈0.1 μm for 80 °C and 0.25 μm for 90 °C (Figure 17b,c). The film thickness determined by XRF and FIB-SEM analyses showed close results. When the electroless deposition (1:2 Ag/Au molar ratio) was performed at 80 °C, the Ag was dominant at the beginning of the process. However, when the deposition process (1:2 Ag/Au molar ratio) was performed at 90 °C, the Au was first detected on the interface. This can be explained according to the electrochemical properties of the metals and the binding energies needed to form metal–Ni and Au–Ag bonding.

The proposed 20-step methodology for effective ELD and characterization of Au, Ag, and Au–Ag films for AM-LPBF AlSi10Mg parts includes three major sections: the AM-LPBF printing process (Figure 18a), the ELD process (Figure 18b), and the full quality characterization of the coating (Figure 18c). The AM-LPBF 3D printing steps are as follows (Figure 18a): (1) materials selection, (2) CAD design, (3) software workflow, (4) object fabrication (printing), (5) post processing, and (6) testing of the printed object. The ELD process steps (Figure 18b) are as follows: (7) functionalization of the surface (–OH/–NH$_2$ termination), (8) surface sensitization (optional), (9) surface Pd activation, (10) Ni–P electroless deposition (optional), and (11) Au, Ag, or Au–Ag electroless deposition. The full characterization of the coating quality includes the use of various measurements and analyses (Figure 18c): (12) dimensions and mass measurements, (13) XRF thickness measurements (14) pilling test, (15) optical profilometry, (16) light microscopy, (17) SEM-EDS analysis, (18) XRD analysis, (19) FIB-SEM, and (20) XPS analysis. It is noteworthy that full-scale characterization is needed only during the development stage of the coating process.
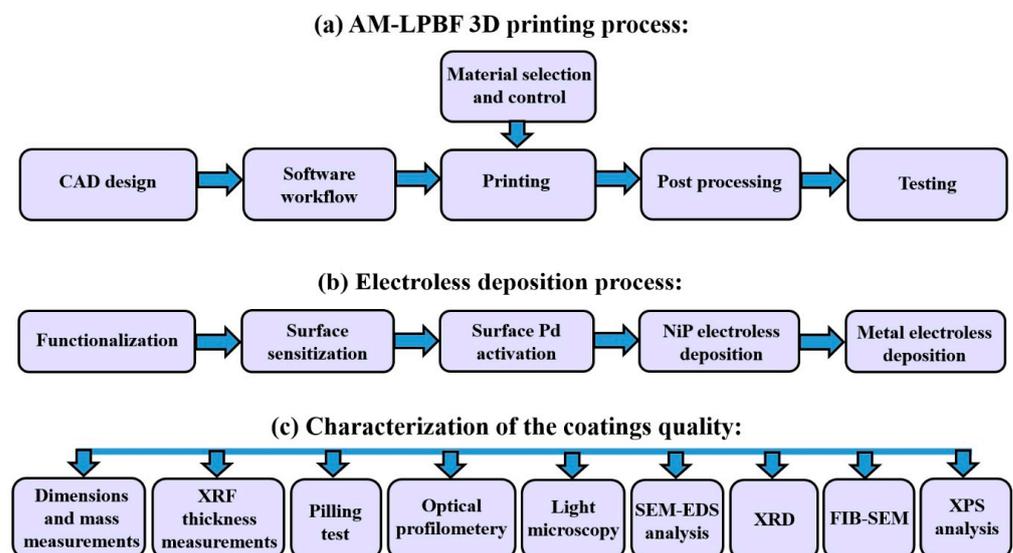
Figure 18. A schematic illustration of a suggested methodology for effective Au, Ag, and Au-Ag electroless deposition (ELD) coatings of AM-LPBF AlSi10Mg parts: (**a**) the AM-LPBF process, post-processing, and quality control; (**b**) the ELD process steps; and (**c**) recommended characterization methods for the analysis of the Au, Ag, and Au-Ag ELD films.

5. Conclusions

Additive manufactured parts frequently need post-printing surface improvement and modification. The aim of this review was to present a novel laboratory-developed environmental-friendly surface finishing process of AM-LPBF AlSi10Mg parts by elec-

troless deposition of Ag, Au, and Au–Ag alloys; a relatively simple, low-cost method allowing the coating of conductive and non-conductive materials. The Ag, Au, and Au–Ag were deposited on as-printed disk-shaped specimens using a dedicated surface activation method, and the coating quality was characterized by various methods. The results revealed that the coatings were composed of crystalline phases or mixed quasi-amorphous and nanocrystalline phases. Similar roughness was observed with and without the use of SAM coating, due to the high roughness of the AM-LPBF AlSi10Mg specimens and the submicron thickness of the SAM film. The optional ≈1 μm Ni–P interlayer improved the adhesion between the substrate and the coated metal, reduced the coated surface roughness, and improved the specimen's overall quality, as shown by the FIB-EDS observations. The roughness of all plated specimens was somewhat reduced as the thickness of the coated layer was increased. In the case of the electrum deposition, at 80 °C, the Ag was dominant at the beginning of the process, whereas at 90 °C, the Au was first noticed on the interface. Adequate quality coatings were obtained for all developed electroless deposition processes. A major advantage of the developed Ag, Au, Au–Ag ELD coatings is the low processing temperature. Another significant benefit of the processes is the avoidance of environmentally hazardous material. The developed finishing processes and the proposed full process methodology are suitable for an effective metallization and can be useful as a post-processing step for many other AM-LPBF printed applications for electrical and thermal conductivity enhancement and to improve the appearance of the part.

References

1.　Li, W.; Li, S.; Liu, J.; Zhang, A.; Zhou, Y.; Wei, Q.; Yan, C.; Shi, Y. Effect of heat treatment on AlSi10Mg alloy fabricated by selective laser melting: Microstructure evolution, mechanical properties and fracture mechanism. *Mater. Sci. Eng. A* **2016**, *663*, 116–125. [CrossRef]

2. Aboulkhair, N.T.; Tuck, C.; Ashcroft, I.; Maskery, I.; Everitt, N.M. On the precipitation hardening of selective laser melted AlSi10Mg. *Met. Mater. Trans. A* **2015**, *46*, 3337–3341. [CrossRef]

3. Zhou, L.; Mehta, A.; Schulz, E.; McWilliams, B.; Cho, K.; Sohn, Y. Microstructure, precipitates and hardness of selectively laser melted AlSi10Mg alloy before and after heat treatment. *Mater. Charact.* **2018**, *143*, 5–17. [CrossRef]

4. Van Cauwenbergh, P.; Samaee, V.; Thijs, L.; Nejezchlebová, J.; Sedlák, P.; Iveković, A.; Schryvers, D.; Van Hooreweder, B.; Vanmeensel, K. Unravelling the multi-scale structure–property relationship of laser powder bed fusion processed and heat-treated AlSi10Mg. *Sci. Rep.* **2021**, *11*, 1–15. [CrossRef] [PubMed]

5. Macías, J.G.S.; Douillard, T.; Zhao, L.; Maire, E.; Pyka, G.; Simar, A. Influence on microstructure, strength and ductility of build platform temperature during laser powder bed fusion of AlSi10Mg. *Acta Mater.* **2020**, *201*, 231–243. [CrossRef]

6. Kusoglu, I.M.; Gökce, B.; Barcikowski, S. Research trends in laser powder bed fusion of Al alloys within the last decade. *Addit. Manuf.* **2020**, *36*, 101489. [CrossRef]

7. Rosenthal, I.; Stern, A.; Frage, N. Strain rate sensitivity and fracture mechanism of AlSi10Mg parts produced by selective laser melting. *Mater. Sci. Eng. A* **2017**, *682*, 509–517. [CrossRef]

8. Zaretsky, E.; Stern, A.; Frage, N. Dynamic response of AlSi10Mg alloy fabricated by selective laser melting. *Mater. Sci. Eng. A* **2017**, *688*, 364–370. [CrossRef]

9. Yang, T.; Liu, T.; Liao, W.; MacDonald, E.; Wei, H.; Chen, X.; Jiang, L. The influence of process parameters on vertical surface roughness of the AlSi10Mg parts fabricated by selective laser melting. *J. Mater. Process. Technol.* **2019**, *266*, 26–36. [CrossRef]

10. Steuben, J.C.; Birnbaum, A.J.; Michopoulos, J.G.; Iliopoulos, A.P. Enriched analytical solutions for additive manufacturing modeling and simulation. *Addit. Manuf.* **2019**, *25*, 437–447. [CrossRef]

11. Whip, B.; Sheridan, L.; Gockel, J. The effect of primary processing parameters on surface roughness in laser powder bed additive manufacturing. *Int. J. Adv. Manuf. Technol.* **2019**, *103*, 4411–4422. [CrossRef]

12. Boschetto, A.; Bottini, L.; Veniali, F. Roughness modeling of AlSi10Mg parts fabricated by selective laser melting. *J. Mater. Process. Technol.* **2017**, *241*, 154–163. [CrossRef]

13. Nahmany, M.; Hadad, Y.; Aghion, E.; Stern, A.; Frage, N. Microstructural assessment and mechanical properties of electron beam welding of AlSi10Mg specimens fabricated by selective laser melting. *J. Mater. Process. Technol.* **2019**, *270*, 228–240. [CrossRef]

14. Park, T.H.; Baek, M.S.; Sohn, Y.; Lee, K.A. Effect of post-heat treatment on the wear properties of AlSi10Mg alloy manufactured by selective laser melting. *Arch. Metall. Mater.* **2020**, *65*, 1073–1080. [CrossRef]

15. Han, Q.; Jiao, Y. Effect of heat treatment and laser surface remelting on AlSi10Mg alloy fabricated by selective laser melting. *Int. J. Adv. Manuf. Technol.* **2019**, *102*, 3315–3324. [CrossRef]

16. Lee, S.; Wajahat, M.; Kim, J.H.; Pyo, J.; Chang, W.S.; Cho, S.H.; Kim, J.T.; Seol, S.K. Electroless Deposition-assisted 3D printing of micro circuitries for structural electronics. *ACS Appl. Mater. Interfaces* **2019**, *11*, 7123–7130. [CrossRef]

17. Kuo, C.-C.; Wang, C.-W.; Lee, Y.-F.; Liu, Y.-L.; Qiu, Q.-Y. A surface quality improvement apparatus for ABS parts fabricated by additive manufacturing. *Int. J. Adv. Manuf. Technol.* **2016**, *89*, 635–642. [CrossRef]

18. Han, Q.; Gu, H.; Soe, S.; Setchi, R.; Lacan, F.; Hill, J. Manufacturability of AlSi10Mg overhang structures fabricated by laser powder bed fusion. *Mater. Des.* **2018**, *160*, 1080–1095. [CrossRef]

19. Inberg, A.; Shacham-Diamand, Y.; Rabinovich, E.; Golan, G.; Croitoru, N. Electroless-deposited Ag–W films for microelectronics applications. *Thin Solid Films* **2001**, *389*, 213–218. [CrossRef]

20. Estrada-Raygoza, I.; Sotelo-Lerma, M.; Ramírez-Bon, R. Structural and morphological characterization of chemically deposited silver films. *J. Phys. Chem. Solids* **2006**, *67*, 782–788. [CrossRef]

21. Asher, T.; Inberg, A.; Glickman, E.; Fishelson, N.; Shacham-Diamand, Y. Formation and characterization of low resistivity sub-100nm copper films deposited by electroless on SAM. *Electrochim. Acta* **2009**, *54*, 6053–6057. [CrossRef]

22. Inberg, A.; Livshits, P.; Zalevsky, Z.; Shacham-Diamand, Y. Electroless deposition of silver thin films on gold nanoparticles catalyst for micro and nanoelectronics applications. *Microelectron. Eng.* **2012**, *98*, 570–573. [CrossRef]

23. Duhin, A.; Inberg, A.; Eliaz, N.; Gileadi, E. Electroless plating of rhenium-based alloys with nickel, cobalt and iron. *Electrochim. Acta* **2015**, *174*, 660–666. [CrossRef]

24. Lelevic, A.; Walsh, F.C. Electrodeposition of NiP composite coatings: A review. *Surf. Coat. Tech.* **2019**, *378*, 124803. [CrossRef]

25. Paunovic, M. Electrochemical aspects of electroless deposition of metals. *Plating* **1968**, *55*, 1161–1167.

26. Shacham-Diamand, Y.; Inberg, A.; Sverdlov, Y.; Croitoru, N. Electroless silver and silver with tungsten thin films for microelectronics and microelectromechanical system applications. *J. Electrochem. Soc.* **2000**, *147*, 3345–3349. [CrossRef]

27. Shukla, S.; Gomathi, N.; George, R. Autocatalytic silver-plating of aluminum radio frequency waveguides with autocatalytic nickel as the undercoat for space applications. *Surf. Topogr. Metrol. Prop.* **2014**, *2*, 045004. [CrossRef]

28. Shacham-Diamand, Y.; Osaka, T.; Okinaka, Y.; Sugiyama, A.; Dubin, V. 30 years of electroless plating for semiconductor and polymer micro-systems. *Microelectron. Eng.* **2015**, *132*, 35–45. [CrossRef]

29. Brenner, A.; Riddell, G. Nickel plating on steel by chemical reduction. *J. Res. Natl. Inst. Stand. Technol.* **1946**, *37*, 31. [CrossRef]

30. Wang, C.; Farhat, Z.; Jarjoura, G.; Hassan, M.K.; Abdullah, A.M. Indentation and erosion behavior of electroless Ni–P coating on pipeline steel. *Wear* **2017**, *376–377*, 1630–1639. [CrossRef]

31. Cui, C.; Du, H.; Liu, H.; Xiong, T. Corrosion behavior of the electroless Ni–P coating on the pore walls of the lotus-type porous copper. *Corros. Sci.* **2020**, *162*, 108202. [CrossRef]

32. Guo, Z.; Keong, K.; Sha, W. Crystallisation and phase transformation behaviour of electroless nickel phosphorus platings during continuous heating. *J. Alloys Compd.* **2003**, *358*, 112–119. [CrossRef]
33. Wang, J.; Wu, Q. The effects of anodic interlayer on the morphology and mechanical performances of electroless Ni–P coating on Al alloy. *Appl. Phys. A* **2017**, *123*, 435. [CrossRef]
34. Tsaia, T.K.; Chao, C.G. The growth morphology and crystallinity of electroless NiP deposition on silicon. *Appl. Surf. Sci.* **2004**, *233*, 180–190. [CrossRef]
35. Ashkenazi, D.; Gitler, H.; Stern, A.; Tal, O. Metallurgical investigation on fourth century BCE silver jewellery of two hoards from Samaria. *Sci. Rep.* **2017**, *7*, 40659. [CrossRef] [PubMed]
36. Fishelson, N.; Inberg, A.; Croitoru, N.; Shacham-Diamand, Y. Highly corrosion resistant bright silver metallization deposited from a neutral cyanide-free solution. *Microelectron. Eng.* **2012**, *92*, 126–129. [CrossRef]
37. Zhang, H.; Shen, L.; Chang, J. Comparative study of electroless Ni–P, Cu, Ag, and Cu–Ag plating on polyamide fabrics. *J. Ind. Text.* **2010**, *41*, 25–40. [CrossRef]
38. Liu, S.; Chen, G.; Prasad, P.N.; Swihart, M.T. Synthesis of monodisperse Au, Ag, and Au–Ag alloy nanoparticles with tunable size and surface plasmon resonance frequency. *Chem. Mater.* **2011**, *23*, 4098–4101. [CrossRef]
39. Hough, R.M.; Butt, C.R.M.; Fischer-Bühner, J. The crystallography, metallography and composition of gold. *Elements* **2009**, *5*, 297–302. [CrossRef]
40. Troalen, L.G.; Tate, J.; Guerra, M.F. Goldwork in ancient Egypt: Workshop practices at Qurneh in the 2nd Intermediate Period. *J. Archaeol. Sci.* **2014**, *50*, 219–226. [CrossRef]
41. Suematsu, Y.; Saito, K.; Koyama, M.; Enokida, Y.; Okura, Y.; Nakayasu, T.; Sukegawa, T. Development of micro-mirror slicer integral field unit for space-borne solar spectrographs. *CEAS Space J.* **2017**, *9*, 421–431. [CrossRef]
42. Dresler, N.; Inberg, A.; Ashkenazi, D.; Shacham-Diamand, Y.; Stern, A. Silver electroless finishing of selective laser melting 3D-printed AlSi10Mg artifacts. *Met. Microstruct. Anal.* **2019**, *8*, 678–692. [CrossRef]
43. Inberg, A.; Ashkenazi, D.; Kimmel, G.; Shacham-Diamand, Y.; Stern, A. Gold plating of AlSi10Mg parts produced by a laser powder-bed fusion additive manufacturing technique. *Prog. Addit. Manuf.* **2020**, *5*, 395–404. [CrossRef]
44. Akben, K.; Timur, S. A study of gold–silver alloy electrodeposited from pyrophosphate-cyanide electrolyte using polyethylenimine-KSeCN additives. *Int. J. Electrochem. Sci.* **2018**, *13*, 3855–3873. [CrossRef]
45. Huang, T. Electrodeposited silver-gold alloy as a sensor for paracetamol determination. *Int. J. Electrochem. Sci.* **2017**, *12*, 11419–11427. [CrossRef]
46. Márquez, K.; Staikov, G.; Schultze, J.W. Electrochemical deposition of Ag, Au and Ag–Au alloys on n-Si(111). *Trans. IMF* **2002**, *80*, 73–78. [CrossRef]
47. Stansfield, G.L.; Johnston, H.M.; Baxter, S.N.; Thomas, P.J. Deposition of Ag and Ag–Au nanocrystalline films with tunable conductivity at the water–toluene interface. *RSC Adv.* **2018**, *8*, 6225–6230. [CrossRef]
48. Inberg, A.; Ashkenazi, D.; Kimmel, G.; Shacham-Diamand, Y.; Stern, A. Gold–silver electroless plating on laser powder-bed fusion additively printed AlSi10Mg parts. *Metals* **2020**, *10*, 557. [CrossRef]
49. Shani, D.; Inberg, A.; Ashkenazi, D.; Shacham-Diamand, Y.; Stern, A. Gold plating on AM-FDM ABS components. *Ann. Dunarea Jos Univ. Galati. Fascicle XII Weld. Equip. Technol.* **2019**, *30*, 43–50. [CrossRef]
50. Olivera, S.; Muralidhara, H.B.; Venkatesh, K.; Gopalakrishna, K.; Vivek, C.S. Plating on acrylonitrile–butadiene–styrene (ABS) plastic: A review. *J. Mater. Sci.* **2016**, *51*, 3657–3674. [CrossRef]
51. Yoshino, M.; Masuda, T.; Yokoshima, T.; Sasano, J.; Shacham-Diamand, Y.; Matsuda, I.; Osaka, T.; Hagiwara, Y.; Sato, I. Electroless diffusion barrier process using SAM on Low-k dielectrics. *J. Electrochem. Soc.* **2007**, *154*, D122–D125. [CrossRef]
52. Ulman, A. Formation and structure of self-assembled monolayers. *Chem. Rev.* **1996**, *96*, 1533–1554. [CrossRef] [PubMed]
53. Schreiber, F. Structure and growth of self-assembling monolayers. *Prog. Surf. Sci.* **2000**, *65*, 151–257. [CrossRef]
54. Ashkenazi, D.; Nusbaum, I.; Shacham-Diamand, Y.; Cvikel, D.; Kahanov, Y.; Inberg, A. A method of conserving ancient iron artefacts retrieved from shipwrecks using a combination of silane self-assembled monolayers and wax coating. *Corros. Sci.* **2017**, *123*, 88–102. [CrossRef]
55. Krusenstern, A. *Galvanotechnik of Noble Metals*; Metallurgy: Moscow, Russia, 1974; p. 91. (In Russian)
56. Werner, K.; Nolze, G. Powder cell—A program for the representation and manipulation of crystal structures and calculation of the resulting X-ray powder patterns. *J. Appl. Cryst.* **1996**, *29*, 301–303.
57. Ashkenazi, D.; Cvikel, D. A journey into the microstructure: Using a multifocal 3D digital light microscope to study archaeological artefacts retrieved from shipwrecks. *Digit. Appl. Archaeol. Cult. Heritage* **2020**, *16*, e00129. [CrossRef]
58. Reiher, T.; Lindemann, C.; Jahnke, U.; Deppe, G.; Koch, R. Holistic approach for industrializing AM technology: From part selection to test and verification. *Prog. Addit. Manuf.* **2017**, *2*, 43–55. [CrossRef]
59. Ngo, T.D.; Kashani, A.; Imbalzano, G.; Nguyen, K.T.; Hui, D. Additive manufacturing (3D printing): A review of materials, methods, applications and challenges. *Compos. Part. B Eng.* **2018**, *143*, 172–196. [CrossRef]
60. Silbernagel, C.; Ashcroft, I.; Dickens, P.; Galea, M. Electrical resistivity of additively manufactured AlSi10Mg for use in electric motors. *Addit. Manuf.* **2018**, *21*, 395–403. [CrossRef]
61. Duhin, A.; Inberg, A.; Eliaz, N.; Gileadi, E. Electroless plating of rhenium–nickel alloys. *Electrochim. Acta* **2011**, *56*, 9637–9643. [CrossRef]

62. Guisbiers, G.; Mendoza-Cruz, R.; Bazán-Díaz, L.; Velázquez-Salazar, J.J.; Mendoza-Perez, R.; Robledo-Torres, J.A.; Rodriguez-Lopez, J.-L.; Montejano-Carrizales, J.M.; Whetten, R.L.; José-Yacamán, M. Electrum, the Gold–Silver Alloy, from the Bulk Scale to the Nanoscale: Synthesis, Properties, and Segregation Rules. *ACS Nano* **2016**, *10*, 188–198. [CrossRef] [PubMed]